Multi-frequency observations and analysis of Abell 1682

Nthabiseng Fortunate Khanye
605577

University of the Witwatersrand

A dissertation submitted to the Faculty of Science, University of the Witwatersrand, Johannesburg, in fulfilment of the requirements for the degree of Master of Science.

Declaration

I, Nthabiseng Fortunate Khanye declare that the thesis titled "Multi-frequency observations and analysis of Abell 1682" is a record of my own work unless otherwise stated. The thesis has not been submitted at any other university or research institute for a degree or examination, the thesis does not contain any other person's data, tables, pictures and writings unless specifically acknowledged and cited in the reference section. The work presented in this thesis was carried out at the University of the Witwatersrand, school of physics from January 2017 to February 2018, under the supervision of Professor Sergio Colafrancesco.

signed :_____

date :_____

Abstract

The radio emissions observed in galaxy clusters is usually attributed to the effects of shocks, turbulence and re-acceleration of relativistic particles in magnetic fields which permeate the cluster atmospheres. Clusters contain different sources of radio emissions ranging from active galactic nuclei (AGN) to enormous regions of diffuse radio synchrotron emission known as radio halos and relics. In this thesis multi-frequency observations are used to study the astrophysical origin and properties of the extended radio emission of the A1682 galaxy cluster detected in the LOFAR Two-metre Sky Survey. The first study of the cluster by The Giant Metrewave Radio Telescope (GMRT) suggested that the cluster might host a candidate radio halo and candidate relics due to its excessive radio emission. We found that the main radio emission is associated to a bright radio galaxy (identified with the source A1304+4649A in the NASA Extragalactic Database) with its bended radio jets/lobes. Since the nature of the candidate relic is not well understood, in the second part of the thesis we explore the possibility of a gravitational lensing galaxy and the annihilation of dark matter particles as possible sources of the diffuse radio emission. Publicly available archival images from low frequency radio surveys (mainly LoTSS, NRAO VLA sky survey and GMRT Sky Survey), millimeter (Planck Legacy Archive), optical (Hubble Legacy Archive) and X-ray observations (Chandra Data Archive) are used for the extensive study of this complex cluster.

Acknowledgments

I would like to thank the South African Square Kilometer Array (SKA) for their financial support throughout my masters degree. I am extremely grateful to my supervisor, Prof. Sergio Colafrancesco whose continuous patience, wisdom and diligent guidance made this project possible. I would like to express my sincere gratitude to Dr Paolo Marchegiani, this thesis would have been impossible without his invaluable assistance and guidance. I gratefully acknowledge the input and suggestions provided by Prof. John Carter on the structure and format of my thesis.

I would also like to thank my two delinquent yet resourceful and insightful teammates and friends Siphiwe Thwala and Charles Takalana whose computational skills and knowledge of astrophysics saved my life more times than I can count. Additional thank you goes to Dr Geoff and Dr Justine Beck for their invaluable assistance with my research and thesis and Dr Dmitry Prokhorov who not only let me use the postdoctoral office printer when we finished our own cartridge but also gave me a very helpful insight when I had lost hope.

I extend my deepest appreciation to the woman who has been supporting and motivating from the beginning of my studies, Mrs Cynthia Kunene. It has been very inspiring and comforting to be in your presence, I will forever be indebted to you. Words cannot express how grateful I am to have my supportive and smart friends who have not only tolerated me more than they should have but have kept me motivated and focused from undergrad, Nonkululeko, Zwimangadzo, Mulweli, Maria, Khanani and Itumeleng.

No words can express how thankful I am to my family for their continuous support especially my dearest mother, Mbokeleng, my uncles and my lovely cousin Nkemiseng. You are all a great inspiration to me, hopefully one day your famous "U tla sebetsa neng?" question will be answered. Finally this acknowledgment would be incomplete without expressing my gratitude to Kagiso Mathaba for his endless support, proofreading my thesis, listening to me complain about how tough school is all the time and getting me all those snacks at stressful times.

This is for my family's greatest inspiration,
my late grandmother who will forever live in our hearts.

Ng'sokeleng "Sjwayi" Khanye

18 May 1951- 26 February 2017

Contents

List of Figures

List of Tables

1 Introduction

Clusters of galaxies are the largest gravitationally bound entities in the universe. They typically contain 100s to 1000s galaxies, making them very good laboratories to study the matter power spectrum, amounts of dark and baryonic matter and the nucleosynthesis of the universe. Clusters are rich in hot X-ray emitting gas and are bound by large amounts of the mysterious dark matter. Some clusters have also been found to harbor non-thermal radio emission resulting from radio galaxies or large regions of diffuse radio emissions that cannot be associated with a particular galaxy or galaxies. The diffuse radio emission has only been detected in less than a 100 clusters and is spread between galaxies in the intra-cluster medium (ICM). The diffuse radio emission observed within the ICM is synchrotron emission which is emitted from cosmic ray electrons spiraling in magnetic fields that permeate the cluster. In fact studies in the radio and X-ray energy bands have revealed that the ICM is a composition of hot plasma, magnetic fields and relativistic particles, although the origin of these cosmic ray electrons and the magnetic fields are still enigmatic. The large regions of diffuse radio emissions can be distinguished as giant radio halos and radio relics depending on their observational properties in the ICM. Radio halos are found in the central regions of their host cluster and are known to have a regular almost spherical morphology while relics are located in the cluster edges and have an irregular elongated morphology. Observations have shown that radio halos and relics are more abundant in galaxy clusters with high X-ray luminosity. The observation of galaxy clusters in different energy bands is very crucial in the field of astronomy and cosmology as it probes different astrophysical properties in the ICM and help with the understanding of the evolution, history and formation of galaxy clusters.

In this thesis we conducted a multi-frequency analysis using publicly available archival images from different surveys to investigate the origin and characteristics of the complex synchrotron emissions observed in the Abell 1682 galaxy cluster. The motivation of this study follows from the GMRT survey where they first observed that the central regions of the cluster might contain a giant radio halo (Venturi et al., 2008, 2013) which might be outshined by a dominant radio galaxy in the cluster. This cluster also contains two other discrete radio emissions of unclear origin located at the south-east and north-west regions of the cluster. These discrete radio emissions are also considered candidate radio relics due to their sizes and positions. We aim to use multi-frequency observation to understand the origin of the diffuse radio emission found in the south east and north-west regions of the cluster. We analyze low and high frequency data to estimate the magnetic field and energy densities of the discrete radio emissions found

in the cluster and to investigate the possibility of the south-east emission resulting from the annihilation of weakly interacting dark matter particles. Previous gravitational lensing results of the galaxy cluster are also used to explore the possibility that the south-eastern emission results from a weakly lensing galaxy.

In this thesis, for all relevant physical quantities we adopt the flat ΛCDM cosmology model with $H_0 = 69.6$ km s^{-1} Mpc^{-1}, $\Omega_M = 0.286$ and $\Omega_\Lambda = 0.714$

1.1 Outline

The work in this thesis is organized as follows:

- In chapter 2 we present an overview on the properties and composition of galaxy clusters. We explain the interesting observations of the ICM in the X-ray, radio, optical and infrared bands. We explain differences between the classes of diffuse emission, their emission mechanisms and discuss the shortcoming of those mechanisms.

- In chapter 3 we discuss the methodology and computational tools used to analyze our radio, X-ray, infrared, optical and submillimeter. All the calculations and error analysis involving the radio data will be explained in detail in latter sections of the chapter. Also, a brief discussion is given on the different telescopes (and their archives) that were used to conduct this research.

- In chapter 4 we first review the previous literature on Abell 1682 to show what is know and unknown about the complex radio emission on the cluster, we also present essential previous weak gravitational lensing analysis of the cluster. We then present our results on the analysis of the cluster at different frequencies and a detailed discussion on the implications of our results. We end by suggesting two possible explanations for the enigmatic emission found in the south-east of the cluster.

- In chapter 5 we give a brief summary of the current issue, our results and conclude our work. We also discuss future work.

2 Clusters of Galaxies

2.1 The intra-cluster medium

Observations of the ICM in different energy bands allow us to probe the various structural phenomenology which occurs within galaxy clusters. The 1960's saw the beginning of the observations of galaxy clusters in the X-ray band after the discovery of luminous X-ray sources in the Virgo cluster (Felten et al. 1966; Byram et al. 1966). Galaxy clusters emit X-ray radiation because they contain thermal intra-cluster gas which is heated due to the infall into the gravitational potential resulting to the adiabatic contraction of the gas in the ICM. The ICM gas represents about 75% of the baryonic matter in the ICM, has very high temperatures of order $T_{gas} \approx 10^7 \backsim 10^8$ K and a very low density of order $n_e \approx 10^{-3}$ to 10^{-4} cm^{-3}. Due to these properties the gas is completely ionized (Cavaliere, Gursky, & Tucker, 1971), with the ions and electrons interacting through their electric fields. The interaction causes the deceleration of the relativistic electrons which leads to the emission of X-ray photons, in a process known as the Bremsstrahlung emission. The Bremsstrahlung emissivity is dependant on both the temperature and the density of the gas, and thus X-ray observations are used to obtain these two characteristics of the ICM. The X-ray spectra of clusters is used to determine their temperatures while the normalization of the spectrum is used to obtain the ICM's density (e.g., the coma cluster in Arnaud et al. (2001)). The study of the temperature of the ICM is essential in the derivation of the gas entropy distribution and in determining the total mass content of the ICM through the hydrostatic equilibrium equations (Zhang et al., 2011).

Relaxed galaxy clusters are identified by a centrally peaked symmetrical X-ray emission which decreases radially as the density of the ICM gas also decreases, while cool-core clusters are identified by a sharp rise in the X-ray surface brightness and a drop in the X-ray temperature in the cluster core. This is because as the ICM gas nears the central regions it relaxes, cools down and becomes denser (Hudson et al. (2010), Peterson et al. (2003), Tozzi and Norman (2001)). The X-ray emission in un-relaxed, merging clusters show a discontinuity in the X-ray brightness and discontinuities in the gas distributions of the cluster such as shock fronts and cold fronts, this is because merging events leave traces on the cluster's gas distribution. Shock fronts result from the compression of the ICM gas by a merger event, this will result in an increase of the cluster's X-ray brightness than its surrounding areas. The ICM gas will also have a higher pressure, temperature and density however shock fronts are hard to detect in the X-ray

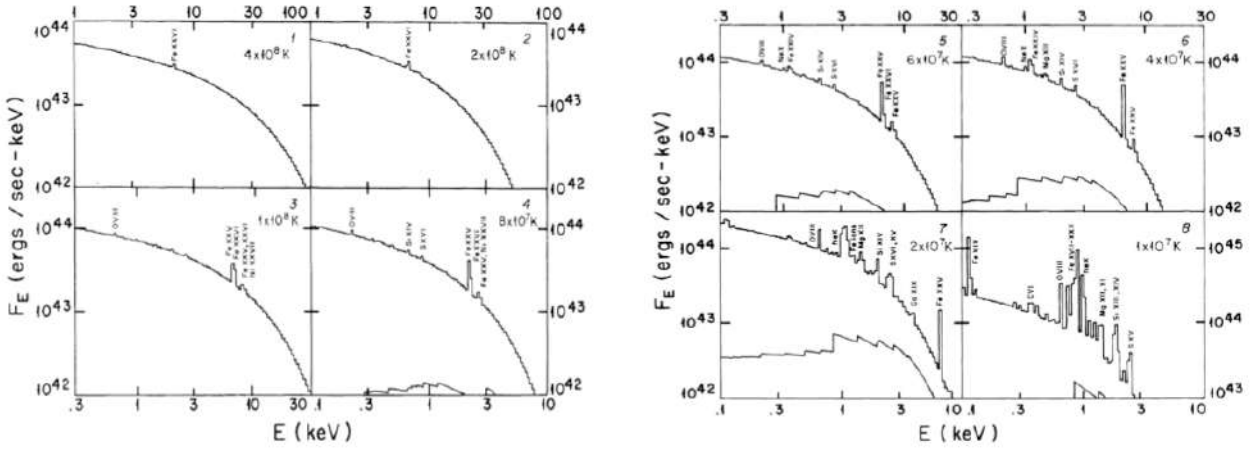

Figure 2.1: The spectra of galaxy clusters in the X-ray energy band, the spectra are arranged from clusters with the highest temperatures (left panel) to clusters with the lowest temperatures(right panel) (Sarazin & Bahcall, 1977)

band as they are often far away from the cluster core (Markevitch et al., 2000; Markevitch & Vikhlinin, 2001, 2007). Cold fronts are caused by the movement of dense, low temperature (cluster's) core regions in the hot ICM gas. This movement results in regions with lower temperatures, high gas density and a roughly equal distribution of gas pressure (Markevitch & Vikhlinin, 2007). Unlike shock fronts, cold fronts appear in both cool core and merging clusters.

The X-ray spectra of clusters is charecterized by the presence of highly ionized elements such as carbon, iron, oxygen sulfur and silicon. The presence of iron in the X-ray spectra was confirmed by Rothenflug and Arnaud (1985) to be a very common feature in the X-ray spectra. Figure 2.1 shows the X-ray spectra of galaxy clusters as studied by Sarazin and Bahcall (1977) using models that explain the ICM gas, all the spectra showed the presence of iron emission line in them and showed that clusters with higher ICM temperature have weaker emission lines compared to the lower temperature clusters. The presence of ionized elements in the X-ray spectra provided evidence of the thermal origin of X-rays in clusters (Mitchell, Culhane, Davison, & Ives, 1976). Because of the prominent levels of gas metallicity, the origin of ICM gas is not cosmological, but it is likely to have resulted from the primoridal gas that has been processed and displaced by galactic winds, supernovae explosion and feedback from active galactic nuclei (AGN).

2.2 The ICM in the optical and infrared band

Galaxy clusters are identified in the optical wavelength through their individual galaxies that observed with optical or infrared imaging and/or spectroscopy. George Abell was the first to catalogue galaxy clusters in 1958 based on their richnesss and their morphology by the visually inspecting photographic sheets from the Palomar Observatory Sky Survey (Abell, 1958, 1965). The clusters were categorized as having regular or irregular morphology. Regular clusters are giant spherically symmetric clusters which normally contain a very large collection of galaxies in the centre and contain spiral galaxies on the cluster edges, they contain a large amount of

Richness classification	number of galaxies	number of clusters
0	30-49	>1000
1	50-79	1224
2	80-129	383
3	130-199	68
4	200-299	6
5	300>	1

Table 2.1: Abell richness classification of galaxy clusters and the number of clusters in each richness class and the number of galaxies in that cluster.

hot gas, an example of a regular class is the Coma cluster. Irregular galaxy clusters take many different shapes and sizes, they lack symmetry and concentration of central galaxies, they can appear as a loose collection of galaxies with multiple centers or as small and large groups of galaxies (Dressler, 1980). An example of an irregular cluster is the Virgo cluster.

The Abell catalogue contains more than 4000 clusters (see table 2.1) and is still used to charecterize and classify clusters. The clusters are named with the prefix A which is followed by the cluster number. Between the years 1961-1968 Zwicky proposed a classification of the clusters as compact, partly compact or open based on their plates and apparent shapes (Zwicky & Herzog, 1968). Bautz and Morgan (1970) further classified clusters according to the degree of domination by the brightest cluster galaxy (BCG). The Bautz-Morgan classification defines three main types of clusters type I, II, III as follows:

- Type I clusters are dominated by a single large, bright core dominant galaxy at the centre e.g., Abell 2199;
- Type II clusters are dominated by one or more intermediately luminous optical galaxy e.g., the Coma cluster;
- Type III clusters are clusters with no dominant galaxy e.g., Virgo cluster.

Galaxy clusters are also observed in the Infrared (IR) band, because IR emission is emitted by any heat radiating astronomical object. In galaxies most of the IR emission is emitted by starlight and is re-processed by IR dust thermal emission. IR galaxies emit radiation in the wavelength range 0.7-350 μm.

2.3 Non-thermal emissions in clusters of galaxies

Up until the late 1950's the most commonly known sources of radio emissions in galaxy clusters were star formations, supernovae activities and the radio emissions from jets that result from AGN activities. However, low frequency observation of some clusters show traces of large scale diffuse and extended synchrotron emissions which are not associated to a specific galaxy or galaxies in the cluster. These large areas of diffuse radio emission, whose origin is still a mystery are grouped into radio halos, radio relics and mini-halos based on their morphology and position within the cluster. In the following sections we will discuss the types of non thermal components found in clusters and the theories (or models) which try to explain their origin.

2.3.1 Active Galactic Nuclei

AGNs are the most powerful and luminous galaxies in the universe, they harbor super massive black holes (SMBHs) which range from 10^8 to 10^{10} solar masses. Although all galaxies contain SMBHs, the SMBHs of AGNs produce unique observational consequences because they constantly accrete matter (gas and dust) into the ICM, they also convert the gravitational energy of this matter into electromagnetic and mechanical energies. The powerful SMBHs also generate an accretion disc around them due to the angular momentum of infalling material, this accretion disc makes it impossible to observe the central regions of the galaxy. There are different types of AGN's ranging from radio galaxies, quasars and Seyfert galaxies.

Radio galaxies

Radio galaxies are a subgroup of AGNs with strong radio emissions, they have a linear double diffuse radio structures which are often symmetrical, these structures are called radio lobes and lie on both sides of the galaxy. The lobes contain narrow relativistic outflows of matter called jets, which connects the core of the galaxy the the lobes. When the jets meet the ends of the lobes there are usually small regions of intense radio emission called hotspots. The core of the galaxy is unresolved and corresponds to the galactic nuclei. In more detail, the main components of radio galaxies are:

- **Core:** this is the compact unresolved region corresponding to the nucleus, this is where the collimated flow of radiation arises. The core has a linear size of 100pc and usually has a flat radio spectral spectrum.
- **Jets:** these are highly collimated beams of relativistic particles which come directly from the galactic nuclei to the lobes, the jets transport radiation from the core to the external regions of the galaxy. They are normally oppositely directed and have a spectral index; $\alpha \sim 0.7$ (where $S \propto \nu^{-\alpha}$).
- **Lobes:** these are the extended low surface brightness elliptical structures positioned outside the nuclei, they are often paired and symmetrical. Lobes have a steeper spectrum; $\alpha \geq 1$ ($S \propto \nu^{-\alpha}$) and may spread over a few Mpc in size (on giant radio galaxies), sometimes they are far more stretched and referred to as plumes (Scheuer, 1974). Lobes contain the oldest population of electrons compared to jets and hotspots.
- **Hotspots:** these are bright smaller structures with a roughly spherical morphology. These structures point towards the direction of the cool flow that comes from the core which is heated and shocked due to its interaction with the external galactic regions.

Radio galaxies are catergorized into two subclasses with respect to their radio power and morphology. There are Fanaroff & Riley type I (FRI) and type II (FRII) radio galaxies (Fanaroff & Riley, 1974):

- **Fanaroff & Riley type I:** these radio galaxies are brightest near the galactic core, as shown on the left side of Figure 2.2. They do not show well defined lobes and do not host hotspots, FRI radio galaxies become gradually fainter until the point where their lobes terminate. Their most luminous component being their jets which are more powerful

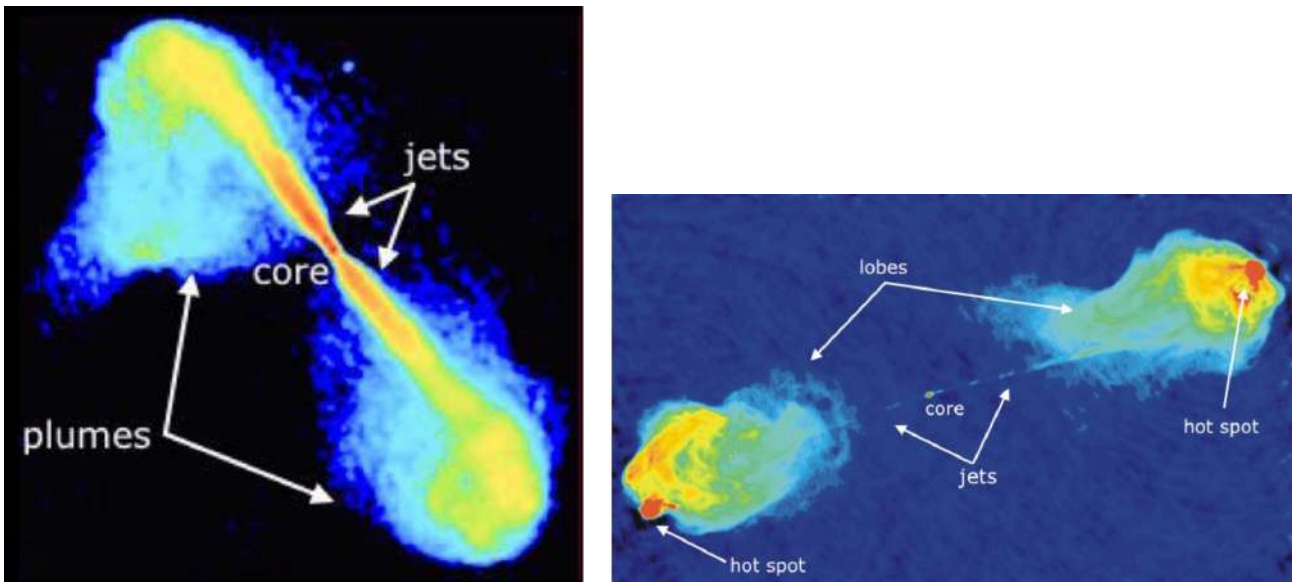

Figure 2.2: The two types of radio galaxies *Left:* VLA false colour image of 3C 296, an FRI type radio galaxy *Right:* False colour VLA image Cygnus A an FRII radio galaxy (credit: R. Perley, C. Carilli and J. Dreher).

than FRII jets and their lobes have a steeper spectrum compared to FRII. FRI jets have a wide range of morphologies, from linear symmetrical double-sided jets to bent 'head-tail' sources. The jets in FRI travel subsonically to the external regions of the galaxy and de-accelerate gradually due to their interaction with the external regions before developing well defined lobes.

- **Fanaroff & Riley type II:** are radio galaxies which have strong, collimated jets and often host hotspots that can extend several kpc away from the core (Rosswog & Brüggen, 2007) as shown on the right side of Figure 2.2. The hotsposts are their brightest regions and the lobes often have an elliptical morphology, unlike FRI the core and the jets of the FRII type are less dominant. FRII jets travel at supersonic speeds and transport energy efficiently until the ends of the lobes, making them brighter in the outside regions of the galaxy.

The symmetric morphology of tailed radio galaxies (FRI and FRII) described above is a common feature amongst isolated galaxies; which is why $\approx 30\%$ of radio galaxies are symmetric while the majority have disturbed morphologies (e.g., O'Dea and Owen, 1985). Radio galaxies are further classified according to the angle, θ, in-between their two jets, the classification differs from head-tail sources (HTs), narrow-angle tails (NATs) to wide-angle tails (WATs) FRI or FRII radio galaxies. In General, WATs have $0^\circ \leq \theta < 90^\circ$ and are typically affiliated with the dominant radio galaxy of the cluster, while the morphology of the jets in HT and NAT radio galaxies are more problematic with the jets bending at an angle of almost 90° and their classification mostly depends on the projection of the jets and angular resolution (Klamer, Subrahmanyan, & Hunstead, 2004). When these radio galaxies were first discovered their strange morphologies were thought to result from the interaction of the radio galaxies with the dense surrounding ICM. NATs are typically affiliated with radio galaxies moving with high

velocities in the gravitational potential of the cluster (Miley, 1980). The ram pressure exerted by the ICM gas is anticipated to be so powerful that it changes the direction of the jets and expel the radio emitting plasma behind the AGN. Optical observations of NAT radio galaxies (e.g., Owen and Rudnick (1976)) show that they are not dominant cluster galaxies and have a faint optical magnitude and low radio luminosity. However, on average, galaxies which host NATs move at velocities equivalent to the velocities of other ordinary cluster objects ($v < 100$ km/s) and so rather than moving at the high unique velocities Bliton, Rizza, Burns, Owen, and Ledlow (1998) suggested that their radio jets might be bent due to bulk motions induced by cluster-subcluster mergers. The physical mechanism responsible for the morphologies of WATs and HTs are also not yet completely understood. Both ram pressure and the buoyancy forces in the active jet may play a role in the distortion of the jets trajectory (Owen and Rudnick (1976); Giacintucci and Venturi (2009)) however optical observations show lower velocities which may not be consistent with the curvatures observed in the radio band (Pinkney, Burns, Ledlow, Gómez, & Hill, 2000). Since NATs and WATs are only found in galaxy clusters, they have been successfully used to select galaxy clusters in radio surveys (e.g., Giacintucci and Venturi (2009))

Quasars

Quasars or Quasi-Stellar Objects (QSOs) are highly luminous AGNs with very broad emission lines in their optical spectra. QSOs appear as point-like sources in the IR and optical observations and since they are highly energetic radio sources they are normally brighter than their host galaxies. Due to their diameter which is typically a fraction of a parsec, QSO's are also known for their high brightness temperatures. Their high energies can be explained by the angle at which they are observed with respect to the line of sight (Urry & Padovani, 1995). QSO's could also be AGNs with a jet pointed directly towards the observer, in this case they are called blazars.

Seyfert galaxies

Seyfert galaxies are spiral galaxies with a very bright core that exhibits broad and narrow emission lines in their optical spectra. Their optical appearance is similar to that of QSO's but not as luminous. The light intensity of the core region of Seyfert galaxies can be compared to the brightness of a Milky-Way like galaxy in other wavelengths (IR and optical). Seyfert galaxies are distinguished by type I and II Seyfert galaxies, type I Seyfert galaxies have both narrow and broad emission lines, while type II Seyfert galaxies only narrow emission lines.

2.3.2 Synchrotron emission

The main source of diffuse non-thermal emission in clusters is synchrotron emission which is produced by relativistic particles spiraling in the magnetic field which permeates the cluster. The origin of these cluster fields is still a mystery and most of what is known about them is derived from the study of diffuse radio emissions and Faraday rotation measures of radio galaxies. Synchrotron radiation is highly polarized and continuous, its strength and frequency are dependent on the strength of the magnetic field.
An electron with energy $E = \gamma m_e c^2$ (where γ is the Lorentz factor, m_e is the mass of an

electron and c is the speed of light), moving at a constant velocity $\vec{v}$ in a spiral cone with a magnetic field $\vec{B}$ will experience a force proportional to $\vec{v} \times \vec{B}$ and emit radiation about the cone's instantaneous velocity. To an observer the radiation will be a continuum signal with a spectrum near the critical frequency v_{synch}, and synchrotron power $\frac{dE}{dt}$ given by equations:

$$v_{\rm synch}[\rm MHz] = \frac{3e}{4\pi m_e^3 c^5}(B_{\rm [G]}\sin\theta)E^2_{\rm [GeV]} \tag{2.1}$$

$$-\frac{dE}{dt}\left[\frac{\rm erg}{\rm s}\right] = \frac{2e^4}{3m_e^4 c^7}(B_{[G]}\sin\theta)^2 E^2_{\rm [GeV]}, \tag{2.2}$$

where θ is the angle between the direction of the magnetic field and the electron's velocity and e is the charge of an electron. If we substitute all the values of all the constants in equation 1.1 and 1.2 we obtain:

$$\begin{aligned} v_{\rm synch}[MHz] &\simeq 16.1 \times 10^6 (B_{\rm [G]}\sin\theta)E^2_{\rm [GeV]} \\ &\simeq 4.2\gamma^2(B_{\rm [G]}\sin\theta) \end{aligned} \tag{2.3}$$

$$\begin{aligned} -\frac{dE}{dt}\left[\frac{\rm erg}{\rm s}\right] &\simeq 6.0 \times 10^{-9}(B_{\rm [G]}\sin\theta)^2 E^2_{\rm [GeV]} \\ &\simeq 1.6 \times 10^{-15}\gamma^2(B_{[G]}\sin\theta)^2, \end{aligned} \tag{2.4}$$

Non-thermal hard X-rays with low and high energies are also expected to be one of the products from the same electrons which produce synchrotron emission through inverse Compton (IC) scattering of the cosmic microwave background's (CMB) photons, but non-thermal X-ray observations have not been confirmed in galaxy cluster. According to equation 2.4 the energy loss rate is proportional to E^2 and so higher energy electrons will lose energy faster than lower energy electrons, this plays and important role in explaining the steep spectrum of diffuse radio emissions.

Using equation 2.3 the Lorentz factor and magnetic fields for electrons in the radio band are estimated to be of order $\gamma \simeq 10^3 - 10^4$ and $B \simeq 1\ \mu$G respectively and for a power-law energy distribution with particle density between $E + dE$ in an isotropic population:

$$N(E)dE = N_0 E^{-\delta} dE, \tag{2.5}$$

where δ is the electron's energy distribution index. In this case the synchrotron emission at frequency, v has a power law spectrum:

$$S_v = v^{-\alpha}, \tag{2.6}$$

where α is the spectral index of the synchrotron emission. α is related to the electron energy distribution index by $\alpha = (\delta - 1)/2$. For an isotropic population of electrons following the power law distribution in a uniform magnetic field it can be shown that the intrinsic linear polarization is given by

$$P_{int} = \frac{\delta + 1}{\delta + \frac{7}{3}} \tag{2.7}$$

however, in observations the degree of polarization detected in diffuse radio emissions, especially radio halos, is much lower than the degree of polarization expected from equation 2.7, which is $\sim 70\% - 80\%$ for typical spectral index values of diffuse radio emission.

2.3.3 Diffuse non-thermal emission in clusters

Radio halos are large areas of diffuse radio emission which are generally located at the cluster center, they have a regular morphology and low surface brightness that ranges from 1 to 0.1 μ Jy/arcsec^2 at 1.4GHz. Radio halos are well known to have a regular spherical morphology that primarily follows the morphology of the X-ray emitting thermal gas; although a number of irregular radio halos which do not trace the morphology of the cluster's X-ray gas have been found (Feretti, Giovannini, Govoni, & Murgia, 2012). The diffuse structures extends over the Mpc-scale in size, however radio halos of smaller sizes have been observed in the MACS J0717.5+3745 (Bonafede et al., 2009) and in the A1351 (Giovannini et al., 2009) galaxy clusters. Halos usually appear to be unpolarized, in fact out of all the known halos only two radio halos, observed in the MACS J0717.5+3745 cluster (Bonafede et al., 2009) and in the A2255 cluster (Govoni et al., 2005) have been detected with filamenatry polarized emission. They are also known to have a very steep spectrum, with $\alpha > 1$ (where $S_v \propto v^{-\alpha}$) and are greatly associated with clusters that show a history of or have ongoing cluster mergers. Giovannini, Tordi, and Feretti (1999) showed that the occurrence of radio halos increases with an increasing X-ray luminosity and temperature of the host galaxy cluster.

Radio relics are also extended diffuse radio emissions similar to radio halos in size ($\geq$ 1 Mpc), steep spectrum ($\alpha \geq 1$, where $S_v \propto v^{-\alpha}$) and low surface brightness except that relics are primarily found in the peripheral regions of the cluster. They have an irregular elongated morphology, with the major axis of the relic roughly perpendicular to the direction of the cluster merger(Feretti et al., 2012). They are highly polarized which indicates a level of organization of the magnetic field in the regions where the relic is present. Unlike radio halos, relics are found in both cool core and merging clusters. They generally trace shock fronts from cluster merger events, this suggests that the relativistic particles responsible for their emission are likely to be re-accelerated and (or) compressed across the cluster by those merger shocks (Feretti et al., 2012).

Mini-halos are mostly located in the central regions of relaxed, cool-core galaxy clusters, they are normally found in clusters with a dominant central radio galaxy. Their radio emission extends beyond the emissions of the dominant AGN but their emission is associated with the ICM and not with the AGN. Mini-halos are also similar to radio halos except that their diffuse emission extends on a moderate scale ($\simeq$ 500 kpc). The classification of mini-halos is very blurry and they are considered as smaller versions of radio halos. Unlike radio halos and relics mini-halos are not easily observable as they are mostly outshined by the dominant radio galaxy at the cluster center. An example of a cluster that hosts a mini-halo is the high X-ray luminous

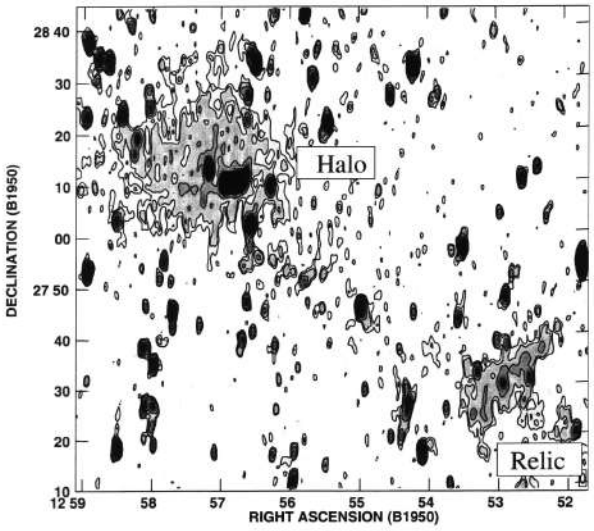

Figure 2.3: WSRT 90cm radio contours of the Coma cluster showing the Coma C radio halo found in the central region of the cluster and the 1253+275 radio relic positioned south west of the cluster, the contours levels are 3, 5, 10, 30, 50mJy/b and the image has a resolution of $55'' \times 125''$ (credit: Giovannini et al., 1993).

cluster RXJ1347.5-1145 which is discussed extensively in Gitti, Ferrari, Domainko, Feretti, and Schindler (2007)

The occurence of non-thermal diffuse emission features very uncommon in clusters as only $\sim 10\%$ of galaxy clusters have been observed to host radio halos and relics, and even fewer clusters host both radio halos and relics simultaneously, while there are only around 20 observed mini-halos. The detection of diffuse extended radio emission is hindered by their low surface brightness, steep spectrum and big sizes. The detection of the diffuse emission also requires a single-dish, highly sensitive (to low surface brightness synctrotron emission) and high angular resolution low frequency telescopes (Feretti et al., 2012), however these parameters are not easy to achieve simultaneously in radio telescopes.
The first detected galaxy cluster containing extended radio emissions was the Coma cluster observed in the late 1950's by Large, Mathewson, and Haslam (1959). Willson (1970) was the first to show that the radio emission in the Coma cluster was diffuse and not associated with any specific galaxy and speculated that the radio emission may be due to the ejection of relativistic particles from the surrounding galaxies. This lead to various extensive studies of the Coma cluster at different radio wavelengths, thus making the Coma cluster the prototype for the study of non-thermal diffuse emissions. Figure 2.3 shows the 90cm diffuse radio emission observed by the Westerbork Synthesis Radio telescope (WSRT) in the Coma cluster. The giant radio halo is clearly visible on the central regions of the cluster and spreads over the top left corner of the radio image (Giovannini, Feretti, Venturi, Kim, & Kronberg, 1993). The Coma cluster also hosts a relic on its peripheral regions, the relic is smaller is size compared to the radio halo. Ever since the detection of diffuse emission in the Coma cluster, many other clusters have been observed to host diffuse radio emissions. This has lead to a great debate on the origin of these sources and so far several theories have been put forward to explain the

origin of the relativistic particles and the magnetic fields responsible for the mechanism that leads to the formation of relics, halos and mini-halos. Synchrotron radiation has been proposed as the underlying mechanism for radio halos, which is produced when relativistic particles are accelerated in a magnetic field in the ICM. Several models explaining the origin of relativistic particles (electrons) and their shortcomings are discussed in detail below, the origin of cluster magnetic fields is also discussed in later sections.

The primary electrons model

This model attributes the radio halo emission to the diffusion of relativistic electrons by different events occurring in the cluster. The injection of relativistic electrons in galaxy clusters may result from galactic winds (or supernovae) which expel charged particles from galaxies into the ICM. The re-acceleration of these relativistic electrons into the ICM may also result from the turbulence and shocks caused by high energy merger events in the cluster (Tribble, 1993; Brunetti, Setti, Feretti, & Giovannini, 2001) and AGN activities (radio galaxies, quasars etc.) can also accrete relativistic electrons into the cluster (Jaffe, 1977). Primary electrons injected by AGN activities and galactic winds suffer strong radiation energy loss and so radio halos are supposed to be a short-term phenomena since relativistic electrons lose their energy quickly ($\sim 10^{7-8}$ yr) therefore re-acceleration of the relativistic particles would be needed to maintain their energy levels in order to be observable(Jaffe, 1977; Brunetti et al., 2001). The re-acceleration of relativistic electrons can be caused by turbulence generated by merger events, their energy is transferred into the synchrotron radiation through resonant interactions of electrons by magnetohydrodynamic (MHD) waves induced by the merger turbulence. Turbulent re-acceleration is like a secondary Fermi process and requires that $(v_{\rm wave}/c)^2 \ll 1$ (where $v_{\rm wave}$ is the velocity of the wave), consequently the mechanism is not completely efficient (Feretti et al., 2012), but it explains the large sizes and mechanism behind radio halos and mini-halos.

The re-acceleration of relativistic electrons can also be caused by the shocks resulting from merger events which can diffusely scatter particles back and forth within the ICM through the mechanism of Diffusive Shock Acceleration (DSA), this mechanism is linked strictly to the presence of radio relics in galaxy clusters. Re-acceleration by shock predicts that the magnetic field within the relic is aligned to the shock front (Enßlin, Biermann, Klein, & Kohle, 1997). This mechanism is a first-order process and is recognized as the mechanism which is responsible for the particle acceleration of supernova residue.

One of the major problems with the re-acceleration models is that the physical mechanisms (e.g., cluster magnetic fields, etc.) that produce the re-acceleration are still not well understood, leaving a high number of free parameters (e.g., acceleration efficiencies, magnetic field profiles etc.), which are often adjusted to fit radio halo properties. Dunn, Fabian, and Taylor (2005) estimated the life time of cluster mergers to be of order $\sim 10^9$ yr which explains why radio halos and relics are so rear, another problem with the primary model is the low level of gamma rays observed in galaxy clusters, strongly limiting the efficiency that these acceleration or re-acceleration processes can have (Vazza, Brüggen, Gheller, & Wang, 2014; Vazza et al., 2016)

The secondary electrons model

This model predicts that secondary relativistic electrons may result from the inelastic hadronic collisions between relativistic protons and protons from the hot gas in the ICM. Through proton-proton collisions, non-thermal electrons are produced and distributed throughout the cluster. Since the lifetime of relativistic protons is of the order of Hubble time and because of the low rates of their radiative (synchrotron and IC Scattering) energy losses, the secondary electrons resulting from the collision can scatter throughout the whole cluster without the need to be re-accelerated. The interaction that leads to the constant injection of secondary electrons is described by equations:

$$\begin{aligned} p + p &\rightarrow \pi^0 + \pi^{\pm} + X \\ \pi^{\pm} &\rightarrow \mu^{\pm} + \nu_{\mu} \\ \mu^{\pm} &\rightarrow e^{\pm} + \nu_{\mu} + \nu_e \\ \pi^0 &\rightarrow 2\gamma, \end{aligned}$$

where p is a proton, $\pi^{0,\pm}$ is a pion, the superscripts indicate the charge of the particle, $\mu^{\pm}$ is a muon and ν_{μ} is the muon neutrino. $e^{\pm}$ indicate is the electron (negative) and positron (positive), ν_e is the electron neutrino and γ indicates the gamma ray particle.

This model also predicts large gamma ray fluxes from the decay of pions which result from the collision, however gamma ray emissions have not been detected in galaxy clusters. The model also predicts the basic properties of radio halos with a regular morphology since relativistic protons can travel larger distances from their source before they lose their energies, but it fails to justify halos with complex morphologies. This model also shows strong radio X-ray correlation ($L_X \propto P_{1.4}^2$, see Feretti et al. (2012)), although there is an increased probability of detecting halos in clusters with high temperatures and X-ray luminosities. Venturi et al. (2008) found that only $\sim 30\%$ of clusters with X-ray luminosities $L_X(0.2 - 2.4 \text{ keV}) > 5 \times 10^{44}$ erg/s at a redshift $0.2 < z \leqslant 0.4$ hosted radio halos. Other problems with the secondary electron model are that radio halos are supposed to be present in all clusters since cosmic ray protons are present in all clusters and it also fails to account for the the spectral steepning of halos at higher frequency (Thierbach, Klein, & Wielebinski, 2003).

The secondary electrons by dark matter annihalation

The annihilation of dark matter particles may result in large quantities of baryonic, hadronic and leptonic particles such as gamma rays, positrons and electrons. This model assumes the lightest, minimal supersymetric dark matter candidate, the neutralino χ, with mass M_{χ}. χ is a linear combination of two supersymetric Higgs bosons (i.e., Higgsinos) and two supersymetric neutral gauge bosons (i.e., gauginos). Neutralinos annihilate inside dark matter halos thus the secondary electrons and positrons produced from the χ annihilation can produce synchrotron radiation when interacting with the ICM magnetic fields. This model explains the spectral steeping of radio halos at high frequencies and also predicts the position of the radio halos to be in the central regions of the cluster, coincident with the cluster's X-ray emissions (Colafrancesco & Mele, 2001). Since dark matter makes up to $\sim 80\%$ of the mass in galaxy clusters the annihilation products are predicted to be much stronger than other cluster emissions, including gamma rays. The gamma ray emissions produced from the annihilation has been predicted to

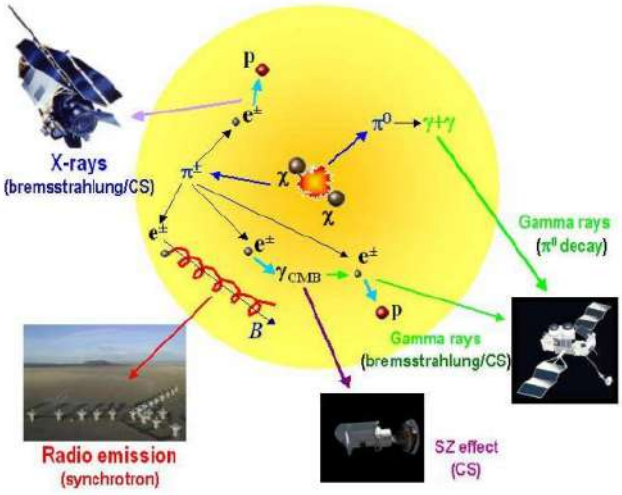

Figure 2.4: Model showing the annihilation mechanism of the lightest, supersymmetric dark matter candindate, the neutralino and the several resulting products including secondary relativistic electrons which produce synchotron radiation. (credit: Colafrancesco (2010)).

extend to energies that correspond to the neutralino mass, which will be tested in future gamma ray observation. Figure 2.4 shows a schematic representation of the neutralino annihilation and the observable products.
The rate of $\chi\chi$ annihilation which leads to the production of electrons and gamma rays is given by:

$$R = n_{\chi\chi}(r) < \sigma v >, \tag{2.8}$$

where $n_{\chi\chi}(r)$ is the neutralino pairs' number density with respect to the radial distribution and $< \sigma v >$ represents the thermally averaged $\chi\chi$ annihilation cross section (Colafrancesco, 2010). The diffusion equation describing the energy loss of the electrons in the magnetized IC plasma produced from the $\chi\chi$ annihilation is given by:

$$\frac{\partial}{\partial t}\frac{dn_e}{dE} = \nabla\left(D(E,r)\nabla\frac{dn_e}{dE}\right) + \frac{\partial}{\partial E}\left(b(E,r)\frac{dn_e}{dE}\right) + Q_e(E,r), \tag{2.9}$$

where $\frac{dn_e}{dE}$ represents the spectrum of the electron, the coefficient $D(E,r)$ represents the spatial diffusion as a function of energy and the radial distribution, $b(E,r)$ represents the electron's energy-loss function and $Q_e(E,r)$ represents the electron's source spectrum (Colafrancesco, 2010). Figure 2.5 shows the radio and gamma ray spectra for the Coma C halo in the Coma cluster obtained from assuming the dark matter annihilation model, the radio spectrum shows a steepening when at high frequencies as predicted by the model (Marchegiani & Colafrancesco, 2016).
Just like the previous models, there are several problems with this model, mostly because of the fact that the nature, mass and composition of dark matter is still a mystery. The cross section of the annihilation and spatial distribution of the halos and sub-halos are difficult to constrain and since every galaxy cluster is bound together by dark matter then radio halos should be detected in almost every massive galaxy cluster. Another problem with this model is that the constraints on the annihilation cross sections that can be derived in other astrophysical sources

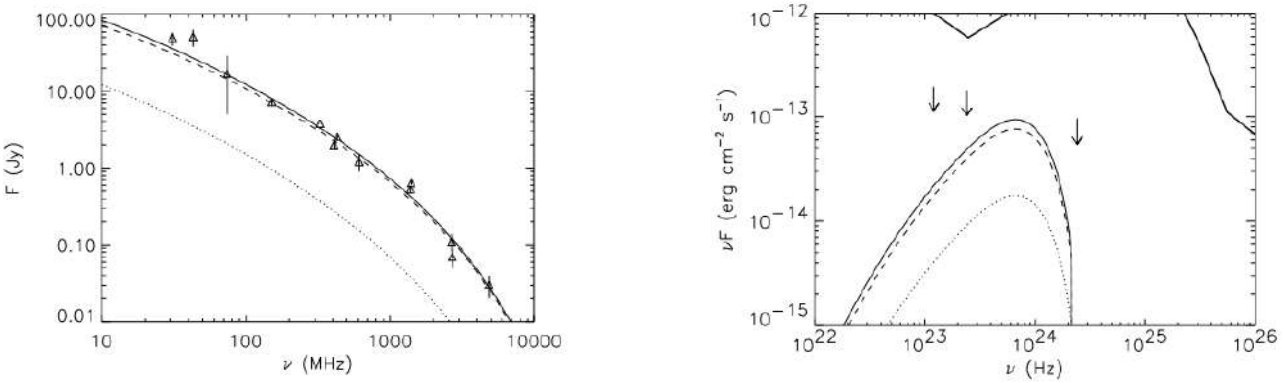

Figure 2.5: Radio (right) and gamma ray (left) spectrum produced by neutralino annihilation for the Coma halos with $M_\chi = 9GeV$ and $\tau^+\tau^-$ composition, in both the spectrums the solid lines show the total emissions, the dashed lines show the contribution of the main halo while the dotted lines of the contribution from the sub-halos (Marchegiani and Colafrancesco (2016)).

can allow us to obtain radio emission from dark matter annihilation in galaxy clusters which are comparable to the currently observed emission only by assuming that the smaller dark matter substructures boost the total emission by a high factor (e.g., Beck and Colafrancesco (2016); Marchegiani and Colafrancesco (2016)). The other problem with this model is that it assumes supersymmetry which has not yet been verified.

2.4 Magnetic fields in galaxy clusters

The study of diffuse radio emissions shows that the ICM is permeated by large scale magnetic fields of order of few μG. Although the origin and role of these cluster wide magnetic fields is still debatable, their presence is demonstrated by the existence of diffuse synchrotron sources in clusters. Cluster magnetic fields are essential in understanding the evolution and history of galaxy clusters as they play a role in cluster dynamics i.e., they play an essential role in the acceleration of cosmic rays and allow us to observe cosmic ray electrons in synchrotron radiation. They also play an important role in determining the structures of galaxy clusters as they restrict processes such as heat conduction, spatial mixing of intra-cluster gas and the propagation of cosmic rays. Even though the origin of galactic and extragalactic magnetic fields is still one of the most challenging problems to explain in modern astrophysics, there are two scenarios which explain the origin of intra-cluster magnetic fields, which are described in detail in Widrow (2002) and Carilli and Taylor (2002) as follows:

- **Galactic scenarios:** in this scenario the ICM is magnetized by galactic winds produced from active and star-burst galaxies or galactic winds from normal galaxies (Rees & Setti, 1968). Galaxy outflows, gas removal processes in galaxies and accretion from AGNs by relativistic outflows (radio jets) all play an important role to the deposition of magnetic fields to the ICM. Matter is also transported into the ICM by galactic winds during the ejection of magnetic fields from galaxies. Galactic magnetic fields also may originate from the magnetic fields of earlier stars which (stellar magnetic fields) are in-turn fed into the interstellar medium by supernovae explosions and stellar outflows. The high degree of

matallicity of the ICM supports this scenario, however magnetic fields in galaxy clusters are much stronger and in some cases larger than galactic magnetic fields. This suggests that cluster fields may be primordial or amplified.

- **Early universe scenario:** according to this scenario, the magnetic fields in galaxy clusters are primordial i.e., their generation could've taken place prior to epoch of recombination. The Biermann battery effect (Biermann, 1950) is one of the mechanisms used to explain the generation of primordial fields, in which weak seed magnetic fields can be generated from zero initial conditions by the relative motion between ions and electrons. This relative motion leads to the generation of thermoelectric currents which create an electric field and a corresponding magnetic field that restores electrostatic equilibrium, the strength of these seed magnetic field are of order $\sim 10^{-21}$ G .

The magnetic field strengths produced by these two scenarios are exceeded by those presently observed in galaxy clusters therefore an amplification mechanism is required. An amplification can occur during cluster mergers and cluster formation processes; the merger shocks, shear flows and turbulence can change the strength and structure of cluster magnetic fields. Turbulence caused by mergers strongly amplifies the magnetic fields intensity in the ICM. Magnetic fields are investigated in the radio band by studying the polarization or the Faraday rotations of radio sources in clusters, they can also be investigated in the X-ray band by studying cold fronts of merging clusters (cold fronts are interpreted as the sharp discontinuities in surface brightness and temperature in the ICM, with the property that the brighter and denser side of the discontinuity is the colder one (see previous sections Markevitch et al. (2000)) and by investigating non-thermal X-rays which originate from the inverse Compton scattering of the CMB photons by cosmic ray electrons. In the following sections we discuss some of the techniques used to measure magnetic fields in galaxy clusters.

2.4.1 Equipartition magnetic fields

This section closely follows Govoni and Feretti (2004) unless stated otherwise.

The equipartition estimation provides a convenient way to calculate the characteristic scale of magnetic fields from synchrotron sources. By assuming the energy densities of relativistic particles ($U_{\rm pr}$ in protons and $U_{\rm el}$ in electrons) and magnetic fields ($U_{\rm B}$) are the same, then the total energy $U_{\rm tot}$ will be minimized giving:

$$U_{\rm tot} = U_{\rm pr} + U_{\rm el} + U_{\rm B}. \tag{2.10}$$

The energy of the magnetic field contained in a source with a volume V is given by:

$$U_{\rm B} = \phi V \frac{B^2}{8\pi}, \tag{2.11}$$

where ϕ is the "filling" factor, which is a fraction of the volume filled by the magnetic field. The electron energy density on the same volume, V, spanning the energy range, E_1 to E_2, can be calculated by assuming the power-law electron energy distribution as in equation 2.5:

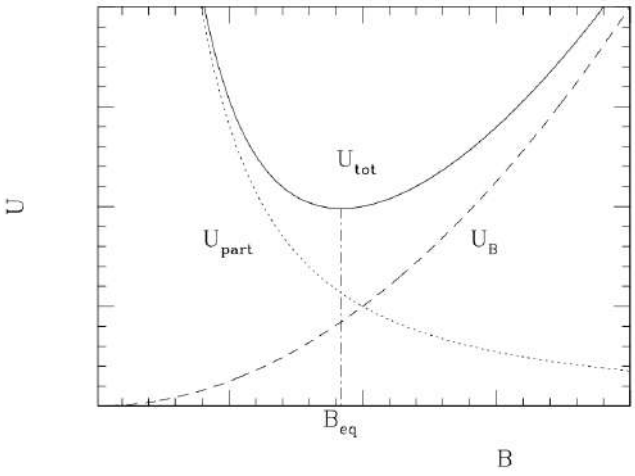

Figure 2.6: The energy contents of a radio source in arbitrary units, $U_{\rm tot}$ is minimum when the energies from the relativistic particles ($U_{\rm part}$) and magnetic fields ($U_{\rm B}$) are almost the same, this is known as the equipartition condition and its corresponding magnetic field is referred to as the equipartition magnetic field. (credit: Govoni and Feretti (2004))

$$\begin{aligned} U_{\rm el} &= V \times \int_{E_1}^{E_2} N(E) E dE \\ &= V N_0 \int_{E_1}^{E_2} E^{-\delta+1} dE, \end{aligned} \tag{2.12}$$

$U_{\rm el}$ can be further expressed as a function of the radio source's synchrotron luminosity, $L_{\rm syn}$, observed between two different frequencies, v_1 and v_2 as:

$$U_{\rm el} = L_{\rm syn} (B \sin\theta)^{-3/2} f(\delta, v_1, v_2), \tag{2.13}$$

where $f(\delta, v_1, v_2)$ represents the function of the index of the electron energy distribution, δ, of the two observing frequencies v_1 and v_2 (see Pacholczyk (1970) for a detailed derivation). If we assume that the proton energy density, $U_{\rm pr}$, is related to the electron energy density $U_{\rm el}$, we can express $U_{\rm pr}$ by:

$$U_{\rm pr} = k U_{\rm el}, \tag{2.14}$$

where k is the ratio of the proton density to electron density. Figure 2.6 shows the energy contents of a radio source with a given synchrotron luminosity, the energy of relativistic particles $U_{\rm part} \equiv (1+k)U_{el}$ is proportional to $B^{-3/2}$ and the energy in the magnetic field U_B is proportional to B^2. The total energy density $U_{\rm tot} \equiv (1+k)U_{el} + U_{\rm B}$ has a fairly sharp minimum near equipartition of the relativistic particle and magnetic densities i.e., where $U_{\rm part} \simeq U_{\rm B}$.
If we take $\sin\theta = 1$, then equation 2.10 becomes:

$$U_{\rm tot} = (1+k) L_{\rm syn} B^{-3/2} f(\delta, v_1, v_2) + \frac{B^2}{8\pi} \phi V. \tag{2.15}$$

The minimum energy, U_{min}, is obtained when the contributions of the relativistic particles and magnetic fields are near equipartition in equation 2.15. This is when $\frac{\partial U_{\rm tot}}{\partial B} = 0$ and thus $U_{\rm min}$ is obtained when:

$$U_B = \frac{3}{4}(1+k)U_{el}. \tag{2.16}$$

$U_{\rm min}$ is known as the equipartition value. By assuming the same volume, V, in magnetic fields and relativistic particles, assuming $\phi = 1$ and applying the K-correction (which "corrects" for the fact that sources observed at different redshifts are, in general, compared with standards or each other at different rest-frame wavelengths. See Hogg, Baldry, Blanton, and Eisenstein (2002) for detailed discussion) then the total minimum energy density, $u_{\rm min} = \frac{U_{\rm min}}{V}$, can be expressed in terms of observable quantities by:

$$u_{\rm min} = \xi(\alpha, v_1, v_2)(1+k)^{4/7} \times v_0^{4\alpha/7}(1+z)^{(12+4\alpha)/7} \times I_0^{4/7} \times d^{4/7}, \tag{2.17}$$

where $\xi(\alpha, v_1, v_2)$ is the equipartition parametrization constant as a function of the spectral index α, between the frequencies v_1, v_2, the constants are tabulated in table 1. on Govoni and Feretti (2004). Here k is the ratio of the total proton energy to the total electron energy, z is the clusters redshift, $I_0\left[\frac{\rm mJy}{\rm arcsec^2}\right]$ is the source's brightness and d[kpc] is the depth of the source along the line of sight. The magnetic field of radio source is then obtained by using the equipartition magnetic field:

$$B_{\rm eq} = \sqrt{\frac{24\pi}{7}u_{\rm min}}. \tag{2.18}$$

It is important to note that the values obtained using the equipartition condition are approximated estimates as there are uncertainties in the results. The value of the ratio k depends on a poorly understood mechanism, the value of ϕ is also uncertain and the line of sight, d, is difficult to infer. Usually the values assumed for galaxy clusters are $k = 1$ or $k = 0$ and $\phi = 1$.

2.4.2 Faraday rotation

The Faraday rotation of radio galaxies is the most direct and promising method for measuring magnetic fields in clusters. Magnetic fields are measured through their effects on the propagation of linearly polarized electromagnetic radiation as it passes through the ICM's magnetized plasma, this is known as Faraday rotation. As the polarized light passes through the magnetized ICM plasma it is subjected to different indices of refraction for different axes depending on the orientation of the magnetic field. The polarized signal which is described by the polarization vector $\vec{p}$, whose intensity, P, and angle, ψ are given by Stokes parameters as:

$$\begin{aligned} P &= \sqrt{Q^2 + U^2 + V^2} \\ \psi &= \frac{1}{2}\tan^{-1}\frac{U}{Q}, \end{aligned} \tag{2.19}$$

where Q, U and V represent Stokes parameters (see Trippe (2014) for derivations). $\vec{p}$ rotates while crossing the ICM plasma before reaching the observer, the intrinsic polarization angle, ψ_{int} will be rotated by an angle:

$$\Delta\psi = \frac{1}{2}\Delta\phi, \tag{2.20}$$

where $\Delta\phi$ is the phase difference between two signals, and so the polarization angle observed will be:

$$\begin{aligned}\psi_{\rm obs}(\lambda) &= \psi_{\rm int} + \Delta\psi \\ &= \psi_{\rm int} + \frac{e^3\lambda^2}{2\pi m_e^2 c^4}\int_0^L n_e\ \mathbf{B}_\parallel \cdot d\mathbf{l},\end{aligned} \tag{2.21}$$

where λ is the wavelength, m_e is the mass of an electron, e is the charge of an electron, $\mathbf{B}_\parallel$ is the component of the magnetic field along the line of sight and n_e is the thermal electron density in the plasma along the line of sight from the source ($\mathbf{l} = L$) to the observer ($\mathbf{l} = 0$). $\psi_{obs}(\lambda)$ is usually expressed in terms of the rotation measure RM:

$$\psi_{\rm obs}(\lambda) = \psi_{\rm int} + \lambda^2 RM, \tag{2.22}$$

where

$$\begin{aligned}{\rm RM} &= \frac{e^3}{2\pi m_e^2 c^4}\int_0^L n_e\ \mathbf{B}_\parallel \cdot d\mathbf{l} \\ {\rm RM}\left[\frac{\rm rad}{\rm m^2}\right] &= 812\int_0^{L_{\rm [kpc]}} n_e[{\rm kpc}]\mathbf{B}_\parallel[\mu{\rm G}]d\mathbf{l}[{\rm kpc}].\end{aligned} \tag{2.23}$$

By convention, RM is negative for a magnetic field pointing away from the observer and positive for a magnetic field pointing towards the observer. $\psi_{\rm obs}(\lambda)$ is an observable quantity. By obtaining multi-frequency polarimetric observations of $\psi_{\rm obs}(\lambda)$, the RM of a synchrotron radiation source can be derived using a linear fit of equation 2.22. The RM values combined with the measurements of the electron density n_e can then be used to estimate the value of the magnetic fields using equation 2.23.

2.5 Dark matter

In 1933, Fritz Zwicky observed that the mass required to keep galaxy clusters gravitationally bound together exceeds the sum of the mass of all the galaxies within the clusters, he calculated that there was an invisible mass $\sim$ 400 times greater than the observed baryonic mass in the Coma cluster (Zwicky, 1933). This is the first evidence for the existence of dark matter, matter that does not emit or interact with baryonic matter, although its existence and properties are studied by its influence on baryonic matter by gravitational effects. In 1970, Vera Rubin and Kent Ford provided the first robust evidence for the existence of dark matter, they found that the galactic rotation curves were flat as a function of radial distance from the galactic center, this indicated that there must be a substantial amount of mass located well beyond where the

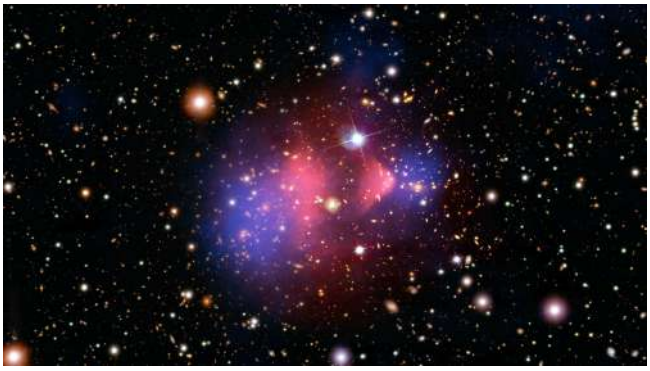

Figure 2.7: The bullet cluster which has an ongoing merger shows evidence for the existence of dark matter (blue) which does not interact with baryonic matter, which is traced by the X-ray emission (pink)

bulk of the visible matter is located (Rubin & Ford Jr, 1970).

A gravitational lensing analysis of the Bullet cluster which has recently underwent a merger event shows unambiguous evidence for non-baryonic dark matter (Clowe et al., 2006). The X-ray emission traces the bulk of the visible matter in the ICM, while a gravitational lensing analysis can provide the mass distribution. In the case of the Bullet cluster, the baryonic matter, which is traced by the X-ray emission, and the bulk of the mass, inferred from lensing observation, are not located in the same place as shown in figure 2.7. This is what's expected in a cluster merger if dark matter only interacts via gravity, while the ionized ICM is subject to both gravitational and electromagnetic forces. Many similar mass analyses of merging galaxy clusters have been performed since this work on the Bullet cluster, and they generally agree with the Bullet cluster analysis (Harvey, Massey, Kitching, Taylor, & Tittley, 2015).

2.5.1 Dark matter particles

There are several constraints from observations (or lack thereof) that any potential candidate for particle dark matter must satisfy. Some of them are listed below:

- Particle dark matter must be "cold", i.e., non-relativistic, because if dark matter particles were "hot", then large scale structures in the universe would form first and smaller structures (like galaxies) would form later. However, observations indicate that structures in the universe form hierarchically from small to large. This implies that dark matter must be "cold" in order to produce all the components of the universe. This requirement rules out the Standard Model neutrinos as a possible dark matter particle, because neutrinos are relativistic and thus "hot".
- In order to explain the observations (or lack of concrete observation so far) from lensing analysis of the Bullet cluster and other clusters, dark matter particles must be uncharged and interact at most very weakly with electromagnetic radiation.
- Finally, a dark matter particle must be stable on cosmological timescales, because if the particle was unstable on timescales shorter than the Hubble time, the bulk of dark matter would have already decayed.

The last two requirements rule out many Standard Model particles as potential dark matter candidates, while there are many candidates that satisfy these constraints, called the Weakly Interacting Massive Particles (or WIMPS). WIMPS are neutral, stable particles that have masses which range on the GeV to TeV scales. One of the reasons that WIMP models are particularly attractive as dark matter candidates is because of a feature of the particles in some WIMP models, such as supersymmetric extensions to the Standard Model (e.g., the neutralino) or Universal Extra Dimensions (e.g., the lightest Kaluza-Klein particle), is that their interaction cross section is on a scale such that they will naturally produce the observed abundance of dark matter in the galaxy clusters and galaxies (Jungman, Kamionkowski, & Griest, 1996; Bertone, Hooper, & Silk, 2005; Hooper & Profumo, 2007).

2.5.2 Indirect detection of dark matter

One of the most interesting characteristics of WIMP candidates is that they can continue to self-annihilate to Standard Model particles. The products of these annihilations commonly yield observable emission in a variety of astrophysical environments across the electromagnetic spectrum (e.g.,Colafrancesco, Profumo, and Ullio (2006)). WIMPs can annihilate to quarks, which hadronize and result in the production of neutral pions, which then decay directly to gamma rays. Secondary gamma-ray production is also possible, as annihilation products can include electrons and positrons, which can then lead to the Inverse Compton scattering of the background radiation, such as the CMB, up to gamma-ray energies. Another scenario is the annihilation of dark matter particles to monochromatic gamma rays (e.g., the final state radiation or internal bremmstrahlung), this would produce a line-like feature at the dark matter particle mass in the gamma-ray energy spectrum, and would be the crucial evidence signal of dark matter (e.g., Rudaz and Stecker (1991)). The observable emission from a dark matter annihilation depends on the total amount of dark matter, the dark matter particle mass and annihilation cross section and the astrophysical emission mechanisms that convert annihilation products into photons. The majority of indirect detection studies focus on gamma-ray emission (or lack thereof) as the observable product of WIMP annihilation. Studies on the gamma-ray emission from the Galactic center (e.g., Hooper and Linden (2011)), diffuse Galactic emission (e.g., Ackermann et al. (2012)), and the isotropic background (Abdo et al., 2010) have been used to constrain different WIMP annihilation scenarios. Additional robust constraints have been derived from the non detection of dwarf spheroidal galaxies (e.g., Geringer-Sameth and Koushiappas (2011); Ackermann et al. (2011, 2014)) and galaxy clusters at gamma wavelengths (e.g., Ackermann et al. (2010); Huang, Vertongen, and Weniger (2012); Arlen et al. (2012)).

2.6 Gravitational lensing

Gravitational lensing is the deflection of light as it passes massive objects such as galaxies or the cluster itself. This deflection results in the apparent change of the observational properties (shape, position and fluxes, excluding surface brightness) of a background source caused by a foreground gravitational lens as witnessed by an observer. Gravitational lensing can be grouped into three classes:

- **Strong lensing:** which occurs when a distant galaxy is directly behind a gravitational mass that can apply a strong gravitational pull, e.g. a massive galaxy or a galaxy cluster.

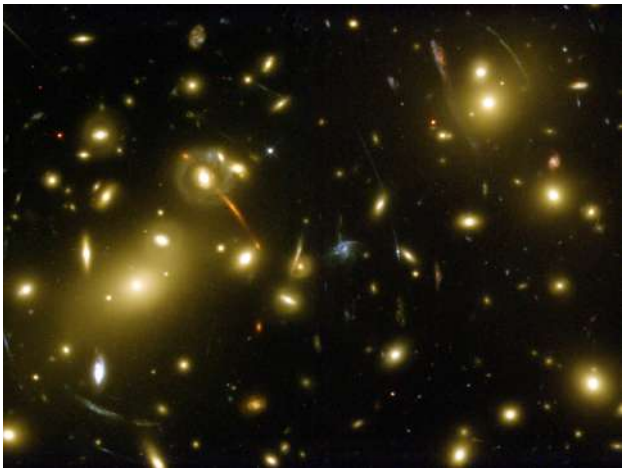
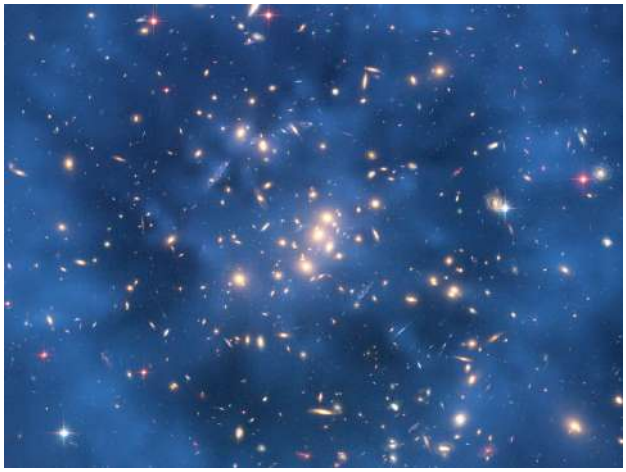

Figure 2.8: Examples of gravitational lensing galaxy clusters *Left:* A2218 shows evidence of strong and weak gravitational lensing. *Right:* CL0024+17 and its dark matter distribution derived from weak lensing analysis (Macario et al. 2013).

This phenomena produces strong distortions in the view of distant galaxies which can result in the formation of multiple images, luminous arcs and Einstein rings of the source. The effects of strong lensing can be easily detected by high resolution telescopes such as the Hubble Space Telescope, an example of strong lensing can be seen on the Bullet cluster.

- **Weak lensing:** which occurs when the light distortion of the distant source by the foreground gravitational lens are small such that we can't easily observe the arcs or multiple images of the background source. Weak lensing is detected by the statistical analysis of the lensing sources, which involves reconstructing the reprojected mass density of the source on the foreground lens. Weak lensing can also be observed in the Bullet cluster.

- **Micro-lensing:** which is caused by the same physical effect as weak and strong gravitational lensing except the lensing source has a smaller mass such as stars and planets. The micro-lensing effect is so small that it can't even be resolved by high resolutions telescopes such as the Hubble telescope, so micro-lensing is studied using photometry by monitoring the the source's brightness fluctuations over a period of time. An example of a cluster with micro-lensing in NGC 6653.

This redistribution of light can be used to measure the mass profile of galaxies and enforces the notion that galaxies are surrounded by haloes of dark matter. Studying the gravitational deflection of light from a background sources helps in mapping the dark matter distribution in the foreground cluster and by using deconvolution and photometry we can estimate the parameters of lensing object.

2.7 The Sunyaev-Zel'dovich effect

In the late 1960's and early 1970s, R.A. Sunyaev and Y.B. Zel'dovich set the ground for what is currently called the Sunyaev-Zeldovich (SZ) effect. The SZ effect is the distortion of the CMB radiation caused by the inverse Compton scattering of photons with hot ionized gas in galaxy clusters (Sunyaev and Zel'dovich (1970), (1972)). As, on average photons gain energy, the blackbody spectrum of CMB shifts to the Wien direction (higher frequencies), which results in an increase in intensity at higher frequencies and a decrease in intensity at low frequencies. The turning point, called the crossover frequency, is around the frequency of $\nu \approx 217$ GHz and for the common cluster parameters, the ratio of SZ intensity to CMB intensity is $\approx 10^{-3}$ which indicates the size of the SZ effect's signal. The SZ effect's signal is independent of the cluster's redshift, this is because the effect is not an emission process but a distortion of the CMB spectrum. As a result for clusters of galaxies of the same mass and electron temperature, the magnitude of the SZ signal is the same for all redshifts. This redshift independence is the reason why the use of the SZ effect as a cluster detection method has an advantage over other detection methods (e.g., optical, X-ray observation, etc) where the flux detactable from the object depends on the luminosity distance, making the high redshift group difficult to detect. The SZ signal does not provide any information on the redshift of galaxies but it can be used to measure the movement and velocities of galaxies in clusters and to probe the properties of the intra-cluster gas allowing us to obtain both thermal and non-thermal properties of clusters (e.g., Colafrancesco, Marchegiani, and Buonanno (2011a)). Since the SZ signal is redshift independent it can also be used to calculate cosmological parameters such as the Hubble constant, the radial perculiar velocity of clusters and the cluster evolution processes (Colafrancesco, 2007; Bahcall & Fan, 1998; Collaboration et al., 2014). An example of clusters where the SZ signal has been detected is the Coma (see figure 2.9) and Bullet clusters (Birkinshaw, 1999). The sources which make the detection of the S-Z signal difficult are noise sources such as the ground noise and other radio source, the detector calibration, the earth's atmosphere and bulk motions within the cluster (Haehnelt & Tegmark, 1996; Carlstrom, Joy, & Grego, 1996; Colafrancesco, 2007)

2.8 Summary

In this chapter we have discussed the phenomenology that occurs in galaxy cluster showing why the study of galaxy clusters is vital in understanding astrophysical and cosmological parameters. We have discussed the importance of both non-thermal and thermal mechanisms that occur in galaxy clusters as they play an important role in understanding the history, evolution and future of the galaxy clusters. In this thesis we are mostly interested in the non-thermal processes such as diffuse radio emission, the interaction of AGNs with the ICM, the annihilation of dark matter particles and gravitational lensing to help us understand the origin and morphology of the complex radio emission found in Abell 1682.

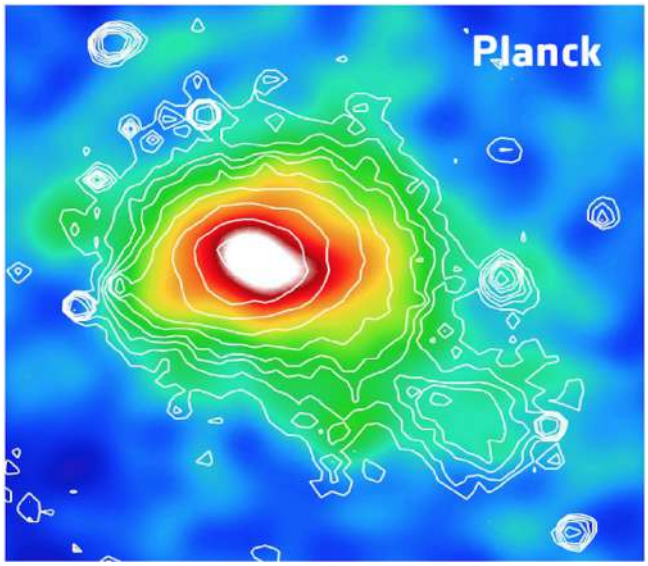

Figure 2.9: The Planck map of the Coma cluster overlaid with X-ray contours measured by the ROSAT survey, showing the SZ effect on the cluster (credit:ESA)

3 Instruments and Analysis

For a comparative and extensive analysis of the origin of the synchrotron emission found in the cluster we used publicly available archival images from radio, infrared, optical, X-ray and Sub-millimeter surveys. This includes four radio observations at different frequencies, initially $10^{'} \times 10^{'}$ cut-out images were retrieved from the LOFAR two metre sky survey (LoTSS) archival image service[1]. We then retrieved radio archival images of the same cluster from the GMRT[2], VLA and NRAO VLA sky surveys[3] (i.e., TGSS, VLSSr and NVSS). Using different radio images is highly essential in understanding the extent and origin of the cluster's synchrotron emission and since the different surveys have different resolutions and sensitivities they enable us to look at the radio spectra, integrated fluxes and to calculate the spectral indices of the radio emissions spread throughout the cluster. The images obtained from the radio surveys were already calibrated, the LoTSS images were direction-dependent calibrated images while the other surveys had direction-independent calibrated images.

To better understand the bimodal nature of the cluster we looked at the relationship between X-ray and radio emission using archival image from Chandra footprint archive [4]. The investigation enables us to determine the relationship between the radio and X-ray sources in the cluster and if they have any connection to the on-going merger in the cluster. The Wide-Field Infrared Survey Exporer (WISE) telescope is famous for its ability to detect objects of high luminosity, its resolution enables the survey to differentiate between luminous objects that overlap in radio and X-ray telescopes and so we used RGB archival images from the WISE data archive [5] to investigate the presence of massive luminous objects capable of producing large scale radio and X-ray emissions in the cluster. An optical band image from the Hubble Legacy Archive[6] was used to find any evidence of gravitational lensing in the cluster and for the comparison of the point sources in the optical band to the radio, X-ray and infrared sources. All of this is done to help in our understanding of the candidate radio relics in the galaxy cluster. A detailed description of the telescopes used for this research is described below.

[1] http://lofar.strw.leidenuniv.nl/doku.php?id=tier1_hba_pdr
[2] http://tgssadr.strw.leidenuniv.nl/doku.php
[3] http://www.cv.nrao.edu/nvss/NVSSlist.shtml
[4] http://cxc.harvard.edu/cda/footprint/cdaview.html
[5] http://irsa.ipac.caltech.edu/applications/wise/
[6] https://hla.stsci.edu/hlaview.html

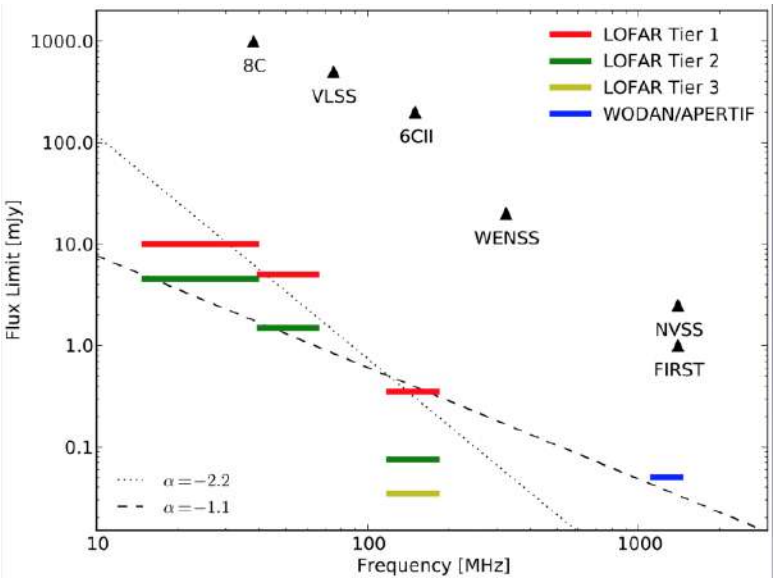

Figure 3.1: A summary of the sensitivity, resolution and frequencies of the the three different LOFAR tiers compared to other known radio surveys (credit T. Shimwell; *http* : *//www.astron.nl/lofarscience*2016/*Documents/Tuesday/LSW_Shimwell.pdf* , page 2).

3.1 Instruments

3.1.1 LOFAR Two-meter Sky Survey

The Low Frequency Array or LOFAR is a very large radio telescope which is sensitive for radio observations below 240 MHz. LOFAR currently receives its data from 24 core stations, 14 of which are in the Netherlands, each with a baseline of about 100km. The LOFAR survey will cover the entire northern sky with over 3,170 antennas which will observe for 8 hours. The project conducts research on three tiers of observations: Tier-1, Tier-2 and Tier-3. Tier-1 is the largest tier and includes high band antenna (HBA, 110-240 MHz) and low band antenna (LBA, 10-90 MHz) observations across the entire northern sky while the Tier-2 and Tier 3 observations will focus on smaller areas with high quality multi-frequency datasets. Figure 3.1 shows the sensitivity, frequency and resolution limits of the different LOFAR tiers compared to other known radio surveys. Due to its unprecedented resolution and sensitivity at low frequency, the telescope will allow us to understand the origin of the relativistic electrons responsible for the diffuse radio emissions found in clusters. This is because LOFAR's sensitivity to low frequency emission enables the study of steep spectral diffuse emission.
The goals of the surveys are:

- To understand the formation of massive galaxies at the epoch of reionisation (EoR) by detection of higher redshift radio sources;
- The study of magnetic fields and hot gas associated with the first bound galaxy clusters and the study of the ICM's magnetic fields;
- The understand of star formation process(es) in nearby and distant galaxies;

- To identify the radio counterparts of sub-mm sources.

Preliminary LOFAR HBA Tier-1 data has been made available online and contains 54 mosaic images which are also available in the image cutout service. The image cutout service contains $1^\circ \times 1^\circ$ calibrated images with typical noise levels of less than 0.5 mJy/beam (or 0.5 mJy/b).

3.1.2 VLA sky survey

The Very Large Array (VLA) Low-Frequency Sky Survey (VLSS) is a radio survey composed of 27 radio antennas, which are 25 meters in diameter, it is located on the plains of San Augustin in New Mexico. The VLSS maps the sky at 74 MHz (4-meter wavelength) and covers the entire sky north of -30° declination at most right ascension. The 27 antennas are mounted on three rail tracks which results in a y-shaped configuration. The survey provides radio images with a resolution of $80''$ and an average rms of ~ 0.13 Jy/b. The VLSS Redux (VLSSr) is the image catalogue containing re-reduced VLSS data, it corrects the flux errors from an incorrect beam and improves the original data from VLSS with new maps which have a $75''$ resolution and an average rms noise level ~ 0.1 Jy/b (see Lane et al. (2014)).

3.1.3 NRAO VLA Sky Survey

The National Radio Astronomy Observatory (NRAO) VLA Sky Survey (NVSS) is a continuum radio survey which covers the whole sky north of -40° declination. The survey maps the sky at a frequency of 1.4 GHz. It has a resolution of $45''$ and a limiting peak source brightness of 2.5 mJy/b and rms noise level of 0.45 mJy/b (Condon et al., 1998). The NVSS contains 217,446 partially overlapping snapshots of radio images and has a catalogue of information on over 1.8million radio sources. The VLSS was initially intended to be the low frequency counterpart to the NVSS for obtaining spectral information of radio source. All NVSS data has been verified and made publicly available on the NVSS data archive.

3.1.4 GMRT Sky Survey

The Giant Metrewave Radio Telescope (GMRT) is an ongoing radio telescope mapping the whole sky north of -30 degrees declination. The array is located 80 km north of Pune in India and is composed of thirty steerable 45 meter (in diameter) parabolic antennas which are spread over a distance of 25 km. Fourteen of the antennas are randomly placed while the rest are placed in a y-shape configuration. The array maps the sky at five different frequencies ranging from 50 MHz to 1450 MHz but its central frequency is 150 MHz with a resolution of $25''$ and rms level of 3.5 mJy/b. The survey has 5,336 number of pointings and a catalogue with over 600,000 radio sources, some of the data collected by the TIRF GMRT Sky Survey (TGSS) has been made publicly available on the TGSS Alternative Data Release (TGSSADR, see Intema, Jagannathan, Mooley, and Frail (2017)), and contains over 5,336 $5^\circ \times 5^\circ$ mosaic images of the surveyed area. The images are also available in the TGSSADR image cutout service. The image cutout service contains $1^\circ \times 1^\circ$ calibrated radio images.
Table 3.1 shows a summary of all the properties of the four radio telescopes discussed in this section.

Name	v (MHz)	Res (")	Noise (mJy/b)	Obs time	reference
LoTSS	141	25	0.5	8 hrs	Shimwell et al. (2017)
NVSS	1400	45	0.45	75 mins	Condon et al. (1998)
TGSS	150	25	3.5	15 mins	Intema et al. (2017)
VLSSr	73.8	75	100	25 mins	Shimwell et al. (2017)

Table 3.1: A summary of they properties of the radio telescopes used in this research. Column 1: shows the telescope name, column 2: shows the telescope's central observing frequency, column 3: shows the telescope's angular resolution, column 4: noise levels (1σ), column 5: is the observation time, column 6: reference.

3.1.5 Chandra X-ray Observatory

The Chandra X-ray Observatory is the X-ray component of NASA's Great Observatory Program, the telescope provides unprecedented sub-arcsecond imaging, spectrometry and a high resolution dispersive spectroscopy of cosmic X-ray sources. The X-ray telescope was launched on the 23th of July 1993, its mass is 4800 kg and it is 10 meters long. The telescope is known for its outstanding image precision, large and perfectly aligned mirrors with a focal length of ~ 10 meters (Weisskopf et al., 2002). The telescope provides images which are 25 times sharper than that of the best previous X-ray telescope. This telescope circulates the earth in an elliptical orbit with the perigee and apogee altitude of 16,800 km and 132,000 km respectively every 64 hours (O'Dell et al., 2000). The energy range of the X-ray observation is 0.1 - 10 keV, and its best resolution is $< 0.5''$. The telescope's maximum effective area is 525 cm^2 at 5 keV. The Chandra Data Archive (CDA) provides the astronomical community with important X-ray data and offers access to Chandra digital archives. The CDA Footprint archive offers calibrated Chandra Observations on a search by object name or position

3.1.6 WISE Telescope

The Wide-field Infrared Survey Explorer (WISE) is NASA's infrared wavelength space telescope, the telescope was launched into space in December 2009 it performs an all-sky survey at four IR wavelengths: 3.3, 4.7, 12 and 23 μ-meters with a field view of 47 arc-minutes wide (Mainzer et al., 2005). The WISE spacecraft has a mass of 661 kg, it is 285 cm tall, 200 cm wide and has a depth of 173 cm and contains a 40 cm wide telescope and four infrared detectors which contain one million pixel each. The space telescope follows a 500 km circular orbit at an inclination of 97.3° and completes its orbit every 94.6 minutes. The telescope's primary goals are:

- To study the evolution, nature and history of ultra luminous infrared galaxies (ULIRG's);
- To identify the most luminous galaxies in the universe;
- To identify brown dwarf (BD) stars in neighboring solar systems and measure their space density, mass function and formation history.

Most of the WISE observations are publicly available on the NASA/IPAC Infrared Science archives and includes an AllWISE Source Catalogue which contains information and 4-band

Figure 3.2: An illustration of the *Left:* Chandra X-ray Observatory. *Center:* WISE telescope in orbit around the earth. *Right:* Hubble Space Telescope in orbit around the earth (credit: NASA)

fluxes on over 747 million galactic objects and the AllWISE Image Atlas with contains 18,240 4-band $1.56° \times 1.5°$ calibrated FITS images (Wright et al., 2010).

3.1.7 Hubble Space Telescope

The Hubble Space Telescope (HST) is the high resolution optical component of NASA's Great Observatory Program. The telescope was launched in April 1990 and has made over 1.3 million observations since it began its mission and it is currently still operational. The telescope has a mass of 11,110 kg and a diameter of 4.2 meters, it circulates the earth in a circular orbit at an apogee and perigee of height of 541 km and 537 km and takes 97 minutes to complete a single orbit. The focal length of the HST mirror is 56.7 m and its wavelength range is 1,100 to 11,000 $\AA$. Its domain is in the ultraviolet, visible and near-infrared frequencies. The primary goal of the telescope was to provide clear and deep views of distant stars, galaxies and our solar system.

3.1.8 Planck All-Sky Survey

The Planck All Sky Survey is a space based mission which was operated by the European Space Agency (ESA). It was launched on the 14th of May 2009 and deactivated on the 23rd of October 2013. The survey was designed to image the temperature and polarization anisotropies of the Cosmic Background Radiation over the whole sky at nine different frequencies ranging from 30 to 857 GHz with two different high frequency instruments (HFI) and low frequency instruments (LFI). The Planck Legacy Archives was made public in 2013 provides public access to the data collected by the Planck Survey, the archive contains temperature and polarization maps, catalogues and cutout images.

3.2 Analysis and methodology

All the images retrieved from the archives are obtained in a Flexible Image Transport System (FITS) file format and were opened and analyzed using different open astronomy data reduction softwares. We used Astropy [7] and its affiliated packages to visualize, edit and create the

[7] http://www.astropy.org/

spectral index map of the radio images, Astropy was also used to compute the infrared and optical RGB images of the cluster. Astropy is a program written in Python, it is designed to be used in astronomy by writing your own source code. The Common Astronomy Software Application[8] (CASA) was used to obtain the radio spectrum, brightness and fluxes from the radio images. CASA is a primary data processing software written in Python and C++, it was developed by the NRAO for calibrating, image processing, editing and enhancement of data for several radio telescopes such as ALMA and VLA.

Before creating the spectral index images we used Miriad [9] to align the NVSS, TGSS and VLSSr radio images so that they cover the same *uv* plane as the LoTSS image. We also used Miriad to smooth the radio images so that they are of the same resolution and position angle. Miriad is a radio interferometry data reduction software created by the Australia Telescope Compact Array (ATCA) for the calibration, cleaning, editing and analysis of radio images (see Sault, Teuben, and Wright (2006) for more details on this software). The images retrieved from the Chandra and Planck archives were visualized, smoothed, scaled and analyzed using DS9[10], an astronomical imaging and data visualization application.

Some of the data used in this thesis is obtained from the ASI Space Science Data Center (SSDC), which is managed by the Italian Space Agency (ASI). The SSDC is a multi-mission science operations, data processing and data archiving center that provides support to several scientific space missions.

In the following sections we explain in details the data analysis of these image using the softwares and programming languages.

3.2.1 Radio images

We firstly retrieved a $10'' \times 10''$ radio image of the A1682 cluster from the LoTSS Prelimenary Data Release Image Cutout Service, where the cluster was observed at 125.3 MHz on the 30th of May 2015. The cutout image had already been flagged, cleaned and calibrated. We then retrieved $12'' \times 12''$ radio images of the same region from the NVSS, TGSS and VLSSr data archives to compare to the LOFAR radio image. The images covered a field larger than the LoTSS image, this is to make sure that their regions overlap with the LoTSS image. The NVSS, TGSS and VLSSr images were observed at 1.4 GHz on the 12th of March 1995, 150 MHz on the 15th of March 2016 and 73.8 MHz on the 20th of September 2003. All the radio images were centered in the position of the dominant radio galaxy.

The $12'' \times 12''$ images are then projected into the LOFAR $10'' \times 10''$ radio images using the "REGRID" function on Miriad. This function handles the conversion from one map projection to another by inputing the image which we want to project (i.e., NVSS, TGSS & VLSSr radio images) and a template image (i.e., LoTSS radio image) which provides the axes, area and coordinates the input images should use. Before these tasks are performed all, the FITS files

[8] https://casa.nrao.edu/

[9] http://www.atnf.csiro.au/computing/software/miriad/

[10] http://ds9.si.edu/site/Home.html

from the radio archives are converted to a different format that is readable by Miriad. This is performed using the "FITS" task on Miriad which converts FITS images to Miriad image files and vice versa. This task was performed for all the radio images including the LoTSS radio image. Once the "FITS" task is performed, we then perform the "REGRID" task on the NVSS, TGSS and VLSSr images using the LoTSS images, this results to 4 four radio images which have the same coordinate descriptors and size ($10'' \times 10''$). The final images each have 67 682 pixels.

3.2.2 Obtaining fluxes and flux errors

Once the images have been re-gridded on Miriad, we used CASA to evaluate the radio fluxes in the four regions containing discrete radio emission. The radio fluxes were obtained using the CASA image interactive tool, this is obtained by running the "VIEWER()" function. Since the radio images had the same size they were opened simultaneously and stacked on top of each other. The LOTSS image was stacked on top and used as a reference. We obtained fluxes from each region at three different beam sizes corresponding to the individual radio telescopes i.e., $25'' \times 25''$ corresponding to the LOFAR and GMRT beam sizes, $45'' \times 45''$ corresponding to the NRA VLA telescope beam size and $75'' \times 75''$ corresponding to the VLA survey's beam size. All the beam shapes in the interactive tool assumed a circular shape, for example the black circular shape at the bottom of figure 3.3 shows the beam size of the telescope (NVSS) used to observe the Abell 800 galaxy cluster, the beam size is $45'' \times 45''$. This outline of the beam size is used as reference when we obtain the integrated flux for a specific area or point source this is because for each pixel CASA calculates the integrated flux in Jy/beam, while for a specified area it calculates the integrated fluxes in Jy. As shown in figure 3.4 the beam size and properties (including the flux density) are defined under the "regions statistics" tab (left image) while all the statistics of the specified region are found under the regions statistics tab (right image) on the CASA interactive viewer. The flux density, S_v, is obtained for all four images at three different beam sizes. The error in the integrated flux density obtained from CASA, ΔS_v, for each region were calculated using the formula:

$$\Delta S_v = \sqrt{(\sigma_{\rm cal} S_v)^2 + (\sigma_{\rm rms}\sqrt{N_{\rm b}})^2}\,, \tag{3.1}$$

where $\sigma_{\rm cal}$ is the uncertainty in the calibration which is assumed to be 10% for all the frequencies, $\sigma_{\rm rms}$ is the rms noise level of the image and $N_{\rm b}$ is the number of beams in the source which we assumed to be equal to 1.

For regions with an integrated flux density value that is less than 3 times the flux noise (S_σ), that flux density value was discarded as it is not a "true detection". We then replaced that flux density value with the $3S_\sigma$ value as an upper limit of the integrated flux density for that specified region. To obtain S_σ the background noise value of each radio image is converted from surface brightness (Jy/b) to a flux density value (Jy) by multiplying it with the telescope's beam sizes using the equation:

$$S_\sigma = \sigma_{{\rm rms},v} \times \frac{\theta^2}{\theta^2_{beam}}, \tag{3.2}$$

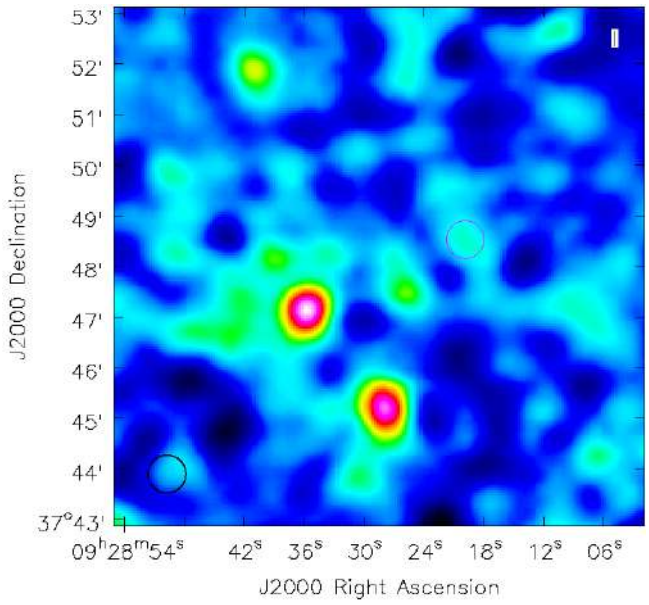

Figure 3.3: A raster (grid of pixels) image of the A800 galaxy cluster opened using the CASA interactive viewer, the black circular shape on bottom illustrates the beam size of the radio telescope. The magenta circular shape is a user defined beam shape used to obtain information on a specific region of the radio image.

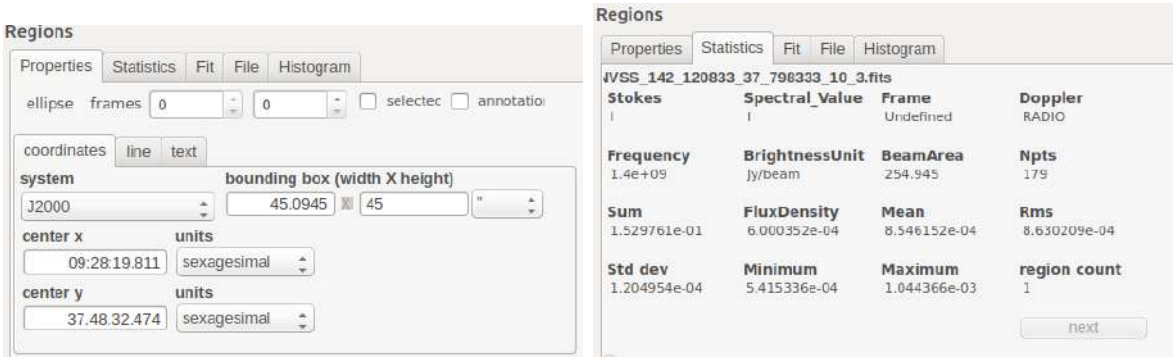

Figure 3.4: An illustration of how radio information on a specific region is obtained using the CASA interactive tool. *Left:* The region properties is used to define the shape, size and position of the beam we want to integrate over, *right:* the region statistics give the radio information of the specified area.

where $\sigma_{\mathrm{rms},v}$ is the noise value of the image at frequency v, θ is the beam we integrated over and θ_{beam} is the beam size of the image at frequency v. The integrated flux densities were used to calculate the spectral index of each region in the cluster using the equation:

$$\alpha_{v_2}^{v_1} = \frac{log\frac{S_1}{S_2}}{log\frac{v_1}{v_2}}, \tag{3.3}$$

where $v_{1,2}$ are the radio frequencies with $v_1 > v_2$ and $S_{1,2}$ are the integrated flux densities corresponding to the frequencies v_1 and v_2. For each region the error of the spectral index between the two frequencies is calculated using the formula:

$$\Delta\alpha_{v_2}^{v_1} = \frac{1}{log\frac{v_1}{v_2}}\sqrt{\frac{\sigma_{1,\mathrm{rms}}^2}{S_1^2} + \frac{\sigma_{2,\mathrm{rms}}^2}{S_2^2}}, \tag{3.4}$$

where $\sigma_{1,2}$ are the rms values of the specified region for frequencies v_1 and v_2.

3.2.3 Estimating the magnetic field and the energy Density

The magnetic field and energy density are also estimated for the discrete radio regions in the cluster using the equipartition condition. To do this we first needed to calculate the radio brightness and spectral index of each region and the source depth. The spectral index was already calculated as discussed in the previous section and the radio brightness of each region was calculated using the formula:

$$I_v = \frac{S_v}{\theta^2}, \tag{3.5}$$

where S_v[mJy] is the integrated flux density of the region at radio frequency v and θ^2[arcsec^2] is the beam area. The beam area for each region was obtained from Ds9 using the regions statistics task. We then used these quantities to estimate the minimum energy density in each region using the equation:

$$u_{min} = \xi(\alpha, v_1, v_2)(1+k)^{\frac{4}{7}} \times v_0^{\frac{4\alpha}{7}} (1+z)^{\frac{12+4\alpha}{7}} \times I_0^{\frac{4}{7}} \times d^{-\frac{4}{7}}, \tag{3.6}$$

where $\xi(\alpha, v_1, v_2)$ is the equipartition parametrization constant as a function of the spectral index α, between the frequencies v_1, v_2, the constants are shown in figure 3.5. k is the ratio of the total proton energy to the total electron energy which we assumed to be $k = 1$ for all regions, z is the cluster's redshift, $I_0[\frac{\mathrm{mJy}}{\mathrm{arcsec}^2}]$ is the regions brightness at $v_0 = 125.3$ MHz and d[kpc] is the depth of the regions along the line of sight. The depth of the regions is calculated using the redshift and beam size. The magnetic field of each region is then obtained by using the equipartition magnetic field:

$$B_{eq} = \sqrt{\frac{24\pi}{7}u_{min}}. \tag{3.7}$$

α	$\xi(\alpha$, 10 MHz, 10 GHz)	$\xi(\alpha$, 10 MHz, 100 GHz)
0.0	1.43×10^{-11}	2.79×10^{-11}
0.1	9.40×10^{-12}	1.63×10^{-11}
0.2	6.29×10^{-12}	9.72×10^{-12}
0.3	4.29×10^{-12}	5.97×10^{-12}
0.4	2.99×10^{-12}	3.79×10^{-12}
0.5*	2.13×10^{-12}	2.50×10^{-12}
0.6	1.55×10^{-12}	1.72×10^{-12}
0.7	1.15×10^{-12}	1.23×10^{-12}
0.8	8.75×10^{-13}	9.10×10^{-13}
0.9	6.77×10^{-13}	6.92×10^{-13}
1.0*	5.32×10^{-13}	5.39×10^{-13}
1.1	4.24×10^{-13}	4.27×10^{-13}
1.2	3.42×10^{-13}	3.43×10^{-13}
1.3	2.79×10^{-13}	2.79×10^{-13}
1.4	2.29×10^{-13}	2.29×10^{-13}
1.5	1.89×10^{-13}	1.89×10^{-13}
1.6	1.57×10^{-13}	1.57×10^{-13}
1.7	1.31×10^{-13}	1.31×10^{-13}
1.8	1.10×10^{-13}	1.10×10^{-13}
1.9	9.21×10^{-14}	9.21×10^{-14}
2.0	7.76×10^{-14}	7.76×10^{-14}

Figure 3.5: Table for the equipartition parametrization constants used to estimate the energy density and magnetic fields (credit: Govoni & Feretti (2004))

3.2.4 Spectral index images

In order to further examine and understand the physical properties of the discrete radio regions observed in the cluster, we constructed a spectral index distribution map of the cluster using images from LoTSS and TGSS with overlapping uv-coverages. We used the Re-gridded TGSS images so that the radio image matches the same area as the LoTSS image, the resolution of the TGSS image was corrected to $25'' \times 25''$ and a position angle $= 22.5°$ so that its position angle and resolution matches that of the LoTSS image. This was done using the "SMOOTH" task on Miriad. The "SMOOTH" task convolves radio images by an elliptical Gaussian function. The spectral index image was created using ASTROPY and its affiliated package, MATPLOTLIB which was responsible for calculating the spectral indices pixel by pixel, plotting the resulting values and plotting the contour lines on the resulting spectral index map. The WCS (World Coordinate System) package was used for the projection and position of the spectral index values on the map. The NUMPY package was used to perform a sigma clipping on values less three times the rms noise for both the LoTSS and TGSS images i.e., regions with values less than three times the rms noise were blanked out. The formula used for the spectral index map was of the form: $S \propto v^{\alpha}$ where S is the surface brightness from the images, v is the frequency and α is the spectral index. The equation used for the spectral index error is:

$$\Delta\alpha = \frac{1}{ln\frac{v_1}{v_2}} \sqrt{\frac{\sigma^2_{1,rms}}{S^2_1} + \frac{\sigma^2_{2,rms}}{S^2_2}}, \tag{3.8}$$

where $\sigma_{1,rms}$ is the rms values of the TGSS image and $\sigma_{2,rms}$ is the rms values of the LoTSS

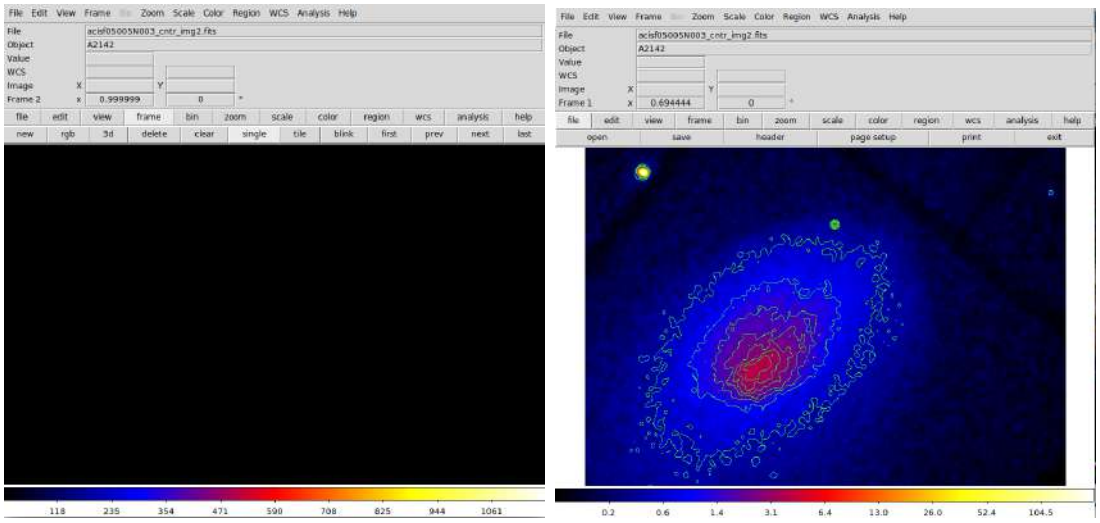

Figure 3.6: The Chandra X-ray image of Abell 2142 before (right) and after (left) statistical adjustments performed using ds9. The X-ray image is scaled using the log scale and smoothed using a Gaussian kernel at $\sigma = 3$ (i.e., $r = 6$).

image, S_1 and S_2 are the surface brightness of the TGSS and LoTSS image respectively.

3.2.5 RGB infrared images

To construct the infrared image of the cluster three RGB FITS files were obtained from the WISE Legacy Archive. The cluster was observed on the 7 June 2010 in four color bands. We used the Astronomical Plotting Library in Python (APLpy) to make the three color RGB cube from the FITS files. This is done by running the "make_rgb_cube()" function which takes the three FITS files with different projections and resolutions and projects them into a single common projection and resolution. The Python Astronomy Visualization Metadata (PyAVM) package was then used to produce an RGB image from the FITS cube, we used PyAVM because it preserves the coordinates and dimensions of the RGB color image, enabling us to superimpose radio and X-ray contours on the infrared image.

3.2.6 Planck and X-ray images

The X-ray and sub-millimeter (sub-mm) image come in more complex FITS format and cannot be easily visualized using CASA, Miriad or Astropy, we thus used the latest version of DS9 to visualize and improve the quality of the X-ray and sub-mm images. The X-ray exposure images are not resolved and consists of instrumental artifacts caused by the imperfection in the mirror and detector of the telescope, this complicates the surface brightness measurements, making it difficult to view the fine X-ray features of a region (see left image of figure 3.6). This is the reason X-ray images require adjustments such as smoothing and scaling. Smoothing the X-ray image helps to bring the finer X-ray properties of the image by removing the statistical noise. We do this by using the "SMOOTH" task on Ds9 and adjusting the smoothing parameters for the image, we selected the Gaussian smoothing kernel which uses the function:

$$z = \frac{1}{\sqrt{2\pi\sigma}} \exp\left[-0.5\left(\frac{x^2}{\sigma^2}\right)\right], \tag{3.9}$$

with

$$\sigma = \frac{r}{2}, \tag{3.10}$$

where x is the counts per pixel, σ is the noise level and r is the kernel radius. After smoothing the X-ray image we then adjusted its scale parameters to adjust the range of the pixel values. We chose the log scale which is defined by the function:

$$y = \frac{log(ax+1)}{a}, \tag{3.11}$$

where x goes from 0 to 1 and a is constant, the default value of a is 1000 and it was not changed for our analysis of A1682. Figure 3.6 shows an example of how Ds9 can be used to visualize and adjust X-ray images using the A2142 galaxy cluster obtained from the Chandra data archive (observation id: 5005). The final X-ray image is plotted using Astropy and is compared to the radio emission found in the cluster by superimposing the LoTSS radio contours on the X-ray image.

The sub-mm image of A1682 obtained from the Planck Legacy Archive was also visualized and adjusted using ds9. The sub-mm image used galactic coordinates and are rotated by an angle of 180° compared to the X-ray and a radio images. We used Ds9 to convert the coordinates format from galactic to J2000 and to rotate the image by 180°. Due to the poor resolution of the Planck telescope the sub-mm image had a poor visual quality and so we decided to also smooth it with a Gaussian kernel of $r = 6$ and adjusted the pixel quality using the log scale function. These adjustments make it easier to analyze the image on the color map.

4 Results and Discussions

In this chapter we present the results obtained from all the observations and analysis discussed in the previous chapter. We first discuss the galaxy cluster in question and what is currently known about it, highlighting the complex morphology of the gas distribution in the cluster. We then present all the results we found including calculations from the annihilation of dark matter particles using previous weak gravitational lensing results.

4.1 What we know about Abell 1682

A1682 is a highly X-ray luminous cluster, $L_{X[0.2-2.4keV]} = 7.02 \times 10^{44}$ erg/s (Venturi et al., 2008), located at a redshift of $z = 0.226$. Previous optical (Morrison et al. 2003) and X-ray (Dahle, Kaiser, Irgens, Lilje, & Maddox, 2002) observations have shown that the cluster has an ongoing merger. Radio observations at 610 MHz performed by the GMRT survey (Venturi et al., 2008) showed that A1682 has a complex radio emission. The authors found that the radio emission on the cluster is dominated by two tail like radio emissions which seem to extend from the central dominant radio galaxy. The tails are labeled as the east tail and the north-west ridge, with regards to their positions on the cluster (see figure 4.1). The authors stated that the east tail (E-tail) might depart from the dominant radio galaxy but were unsure of the origin of the north-west ridge (N-W ridge), they then hypothesized that the N-W ridge might be associated to another radio galaxy but they couldn't confirm this hypothesis. Other than the two tailed like emissions, the authors also observed diffuse radio emission south east of the cluster which is not related to the radio galaxy. This radio emission is labeled as the south-east ridge (S-E ridge) and its origin is also unclear. At 610 MHz the GMRT survey also observed positive radio residuals that spread all around the cluster center, the positive residuals are spread over a region of $\sim 4'$. The diffuse emission was measured to have a flux of $S_{610} = 4.4$ mJy after the subtraction of the point sources, the central tail-like emissions and the S-E emission. The positive residuals are believed to be connected to the ongoing cluster merger and might suggest an underlying radio halo; which might be outshined by the dominant radio galaxy, thus the authors concluded that the cluster hosts a candidate radio halo. The authors also concluded that due to the lack of optical counterparts for the N-W and S-E ridges they may also be connected to the ongoing merger and were classified as candidate relics. Figure 4.1 shows the 610 MHz radio contours overlaid on the Sloan Digital Sky Survey (SDSS) optical image. All the radio

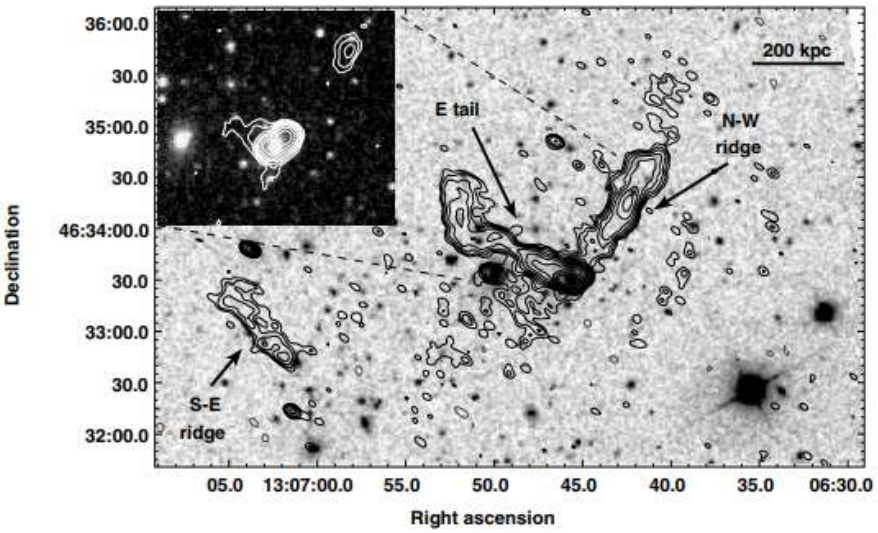

Figure 4.1: The radio contours of A1682 at 610 MHz as observed by the GMRT survey, the contours are superimposed to the SDSS optical red image at a resolution of $6.2'' \times 4.1''$. The insert image shows the radio contours of the cluster at 1.4 GHz as observed by the FIRST Survey, the contours are overlaid on the SDSS optical image at a resolution $1.5''$ (Venturi et al. 2008).

features are clearly distinguishable from the positive radio residuals which spread all over the galaxy cluster. Except for the radio emission surrounding the main radio galaxy these radio features are not visible at 1.4 GHz and seem to be visible at lower frequencies, this emphasizes the importance of lower frequencies for the observation of low brightness, diffuse radio emission. After the inspection of the central regions of the cluster on the FIRST 1.4 GHz image Venturi et al. (2008) also indicated that the radio emission observed on the 1.4 GHz NVSS image seems to result from the convolution of discrete radio sources in the cluster.

Numerous follow up studies of this cluster at 240 MHz (Venturi et al., 2013) and 153 MHz (Macario et al., 2013) also showed a dominant radio galaxy in the cluster's central regions and its associated extended tail (E-tail), the two structures labeled S-E and N-W ridges and an excess of low surface brightness diffuse radio emission which might suggest an underlying radio halo. At these lower frequencies the observations revealed the existence of another interesting radio feature, a diffuse radio emission component which occurred in-between the dominant radio galaxy and the S-E ridge. The structure is labeled as the "diffuse component" and the authors hypothesized that it might be the brightest part of the underlying (candidate) radio halo or it can originate from a dying radio galaxy (Venturi et al., 2013; Macario et al., 2013). Figure 4.2 shows the radio emissions at 240 MHz and 153 MHz for the A1682 cluster, these lower frequency images show the "diffuse component" which was not observed on the 610 MHz GMRT observations. The diffuse component on the 240 MHz image and 153 MHz was found to be coincident to a similar feature on the VLSSr 73.8 MHz radio image. An analysis of this feature showed that it had a very steep spectrum with radio fluxes ranging from $S_{240MHz} = 46 \pm 4$ mJy to $S_{153MHz} = 98 \pm 20$ mJy after the subraction of the point sources in the cluster (Venturi et al., 2009, 2013).

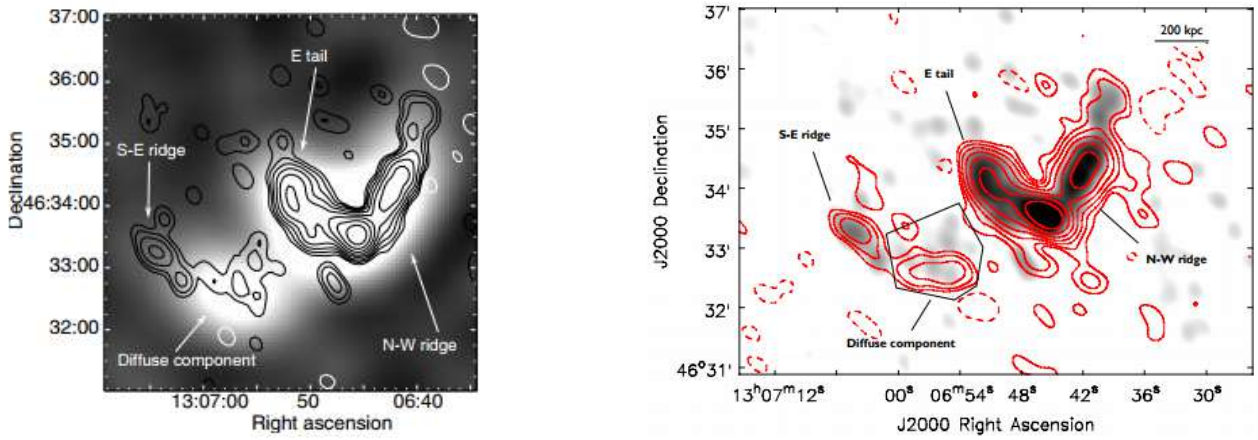

Figure 4.2: *Left:* The radio contours of the A1682 cluster at 240 MHz as observed by the GMRT survey, the contours are overlaid on the VLSSr 73.8 MHz radio emission image of the cluster (Venturi et al. 2012). *Right:* The red contours are 153 MHz GMRT radio contours of the cluster at a resolution of $29.5'' \times 18.0''$ and a position angle of 53.8°, the contours are overlaid on the grey scale 240 MHz image (Macario et al., 2013).

Further LOFAR HBA and LBA preliminary observations of the cluster at 44MHz and 113MHz also show that A1682 is a very steep radio emission cluster. The observations also showed the same features that were observed on Venturi et al. (2008, 2013) for this cluster. The S-E ridge was clearly visible at both the 116 MHz HBA and 44 MHz LBA observations with a very steep spectral index $\alpha_{\rm HBA}^{\rm LBA} \sim$ -2.2. The N-W ridge and East tail are also clearly visible extending from the core of the dominant radiogalaxy with a spectral steepening ranging from $\alpha_{\rm HBA}^{\rm LBA} \sim$ -0.5 to -1.5. The 44 MHz and 113 MHz observations also showed the presence of the positive residue associated with the candidate radio halo. The presence of an ultra steep spectrum radio halo (USSRH) in the cluster would confirm the importance of low radio frequency (radio frequencies ranging a few hundred MHz) observations for the detection of new diffuse cluster emission and would confirm the USSRH in this cluster as the largest and steepest radio halo discovered so far (Venturi et al., 2009).

X-ray observations of the cluster show a discontinuation between the radio and X-ray emission (Dahle et al., 2002; Venturi et al., 2008). The X-ray emission is spread throughout the cluster, however there seems to have no relationship to the bulk radio emission of the cluster, the East tail and N-W ridge are located on the brightest region of the X-ray emission while the S-E ridge is located on the least bright X-ray region. The positive radio residuals however, are spread throughout the X-ray emission.

Beyond the complex radio and X-ray emission A1682 is a weak gravitational lensing galaxy cluster. Lensing observation have found several weakly projected structures in the cluster. Figure 4.3 shows the radial arc found in the cluster after using photometry and statistical analysis on the Hubble Space telescope WFPC2 archive images of the cluster, this study was done by Sand, Treu, Ellis, and Smith (2005). The arcs are revealed after performing a galaxy subtraction, the subtraction then leaves lensed structures such as radial or tangential arcs which may

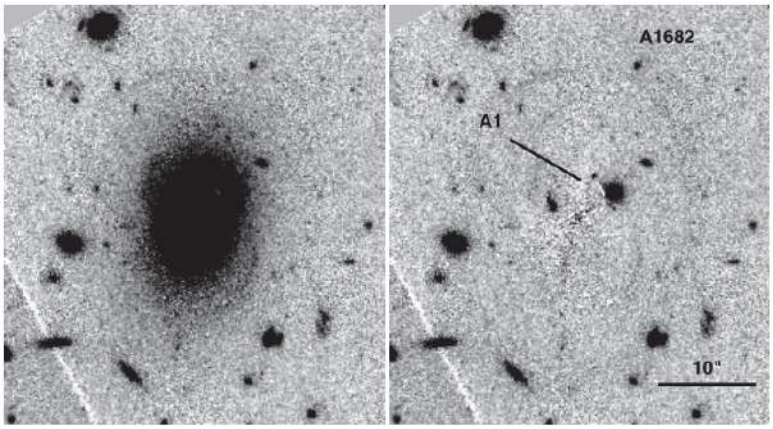

Figure 4.3: The radial arc finding of a region in A1682, resulting from weak gravitational lensing.

ID	R.A(J200) hh mm ss	Dec(J200) ° ′ ″	M_{200} ($\times 10^{14} M_{\odot}$)	R_v (Mpc)
1306_1	13 06 56.1	+46 31 27	$20^{+1.9}_{-1.8}$	$2.5^{+0.1}_{-0.1}$
1306_2	13 06 59.5	+46 33 31	$7.4^{+1.8}_{-1.7}$	$1.6^{+0.1}_{-0.1}$
1306_3	13 07 05.5	+46 30 36	$6.2^{+2.2}_{-2.0}$	$1.2^{+0.1}_{-0.2}$

Table 4.1: The position of the halo mass overdensities due to the lensing effect observed by Ammons et al. 2013 and their properties in a beam dominated by A1682. Col. 1: Notation to differentiate the separate halos in the beam. Col. 2 &3: gives the position of the halos. Col. 4: The projected mass. Col. 5: virial radius.

be magnified in size. The left image of Figure 4.3 shows the brightest cluster galaxy (BCG) which is along the line of sight of a background weak lensing galaxy, the left image shows the radial arc found after performing the BCG subtraction on the Hubble image. The arc is labeled A1, however there was another radial arc found in the cluster, larger than A1 which is not shown in the image.

Ammons, Wong, Zabludoff, and Keeton (2013) used the projected structures caused by weak and strong gravitational lensing effects to derive cluster scale magnification maps (see figure 4.4) and as a result detected three large (dark matter) halo masses at different redshift along the line of sight dominated by A1682. Table 4.1 shows the properties and positions of the halos masses found in the the cluster from the weak lensing analysis of the galaxy cluster. The authors also found two new strongly lensed arc candidates in the cluster after imaging the cluster with the Subaru Suprime-Cam optical telescope [1] (see Ammons et al. (2013)). Dahle et al. (2002) used a weak lensing analysis of the cluster to study the galaxy distribution, the galaxy number density and to reconstruct the gravitational lensing mass distribution of the background source/s in the A1682 cluster and other galaxy clusters using the weak shear caused by weak gravitational lensing.

In the following section we will focus our attention finding the the origin of the complex radio emission in the cluster, mainly the S-E and N-W ridges, using multi-frequency and weak lensing

[1] see https://www.subarutelescope.org/Introduction/instrument/SCam.html for more information on the optical telescope

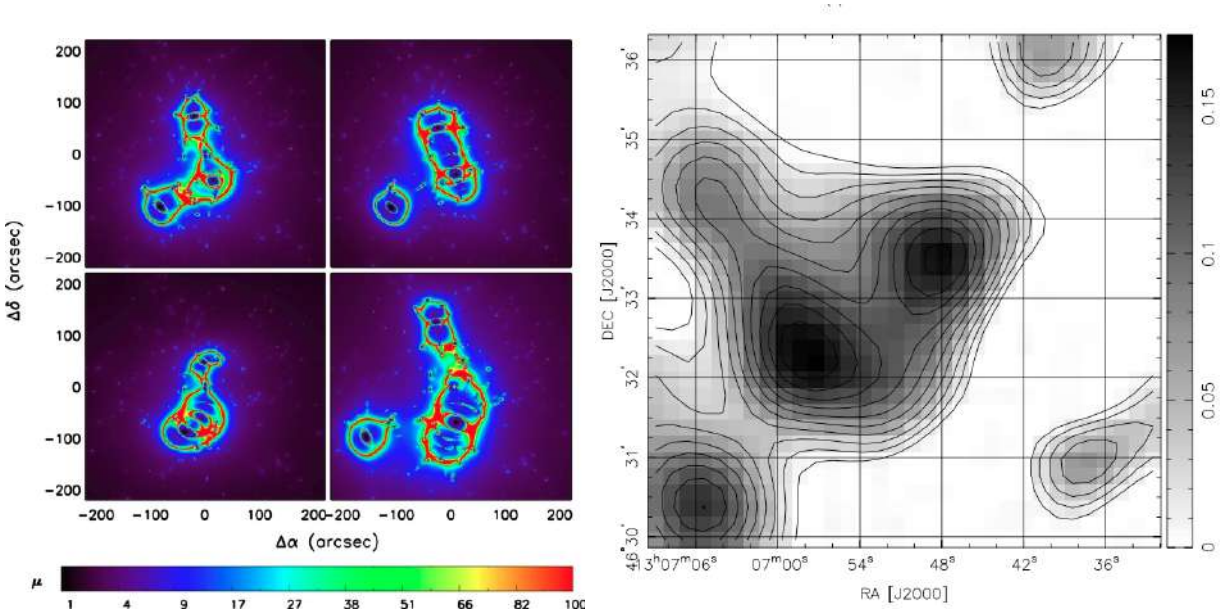

Figure 4.4: *Left:* Monte Carlo 2D lens magnification maps for halos of different mass, centroid and radius created using strong and weak lensing observation in the field of view of A1682 (credit: Ammons, Wong, Zabludoff, and Keeton (2013)). *Right:* the lensing mass distribution map show derived from the weak lensing analysis of the A1682 cluster (credit: Dahle et al. (2002)).

analysis.

4.2 Radio Observations

The noise levels of the radio images (excluding the point sources) are: $\sigma_{\mathrm{LoTSS}} = 0.00322$, $\sigma_{\mathrm{NVSS}} = 0.00053$, $\sigma_{\mathrm{TGSS}} = 0.0047$ and $\sigma_{\mathrm{VLSSr}} = 0.09416$ Jy/b for the LoTSS, NVSS, TGSS and VLSSr images respectively. While rms values for the radio images including all the point sources are: $\sigma_{\mathrm{LoTSS,rms}} = 0.0272$, $\sigma_{\mathrm{NVSS,rms}} = 0.01097$, $\sigma_{\mathrm{TGSS,rms}} = 0.0288$ and $\sigma_{\mathrm{VLSSr,rms}} = 0.396$ Jy/b including all point sources. All the radio images discussed in Chapter 3 are shown in Figure 4.5.
The NVSS contours are in white and are from 0.01097 Jy/b to 0.3 Jy/b in multiples of 2 $\times$ 0.01097, the TGSS radio contours are in black and are from 0.0288 Jy/b to 0.3Jy/b in multiples of 2$\times$ 0.0288 and the VLSSr contours are form 0.396 Jy/b to 3Jy/b in multiples of 0.369. The resolutions of the radio images are $25'' \times 25''$ for the LoTSS and TGSS images, $45'' \times 45''$ for the NVSS radio image and $75'' \times 75''$ for the VLSSr image.

For better comparison of the radio images and in reference to the first GMRT survey study of the cluster, figure 4.6 shows the LoTSS 125.3 MHz radio images with radio contours from the other surveys (left image). The right image shows the same 125.3 MHz with the labels of the discrete regions from figure 4.1 and the positions of the dark matter haloes derived from the weak lensing analysis of the galaxy cluster.

The radio observations all show that there are large concentrations of radio emission in the central regions of the A1682 cluster. The NVSS observation show the radio emission from the dominant radio galaxy and does not show the two tail-like emissions (the East tail and N-W ridge), the S-E ridge and the diffuse emission as observed in figure 4.1 at 610 MHz. The VLSSr image also shows radio emission from the central radio galaxy with the emission extending beyond the radio galaxy's core regions, however it does not distinctly resolve the two tail-like emissions. The image does not show the S-E ridge but we can clearly see the "diffuse components".
The images from the TGSS and LoTSS observations show the same features. Both radio images reveal the central radio galaxy accompanied by two tail-like emissions, the S-E ridge and the positive radio residual spread all over the center of the cluster. The S-E ridge spans over a region of $\sim$ 350 kpc and is not related to the radio galaxy. Like the NVSS radio image the TGSS and LoTSS images do not reveal the presence of a "diffuse component" as observed by Macario et al. (2013) and (Venturi et al., 2013).

A close inspection of the radio images reveal that the radio emission in the cluster is dominated by the central AGN. It is clear that the E-tail is a radio lobe from the radio galaxy, however there are no radio signatures which might suggest the presence of concealed another radio galaxy.

4.2.1 Radio analysis

Table 4.2, 4.3 and 4.4 show the integrated radio fluxes and spectral indices of the discrete radio regions found in the cluster at three different beam sizes. The flux density values, S_ν (where ν is the observed frequency), were obtained and calculated as explained in Chapter 3.

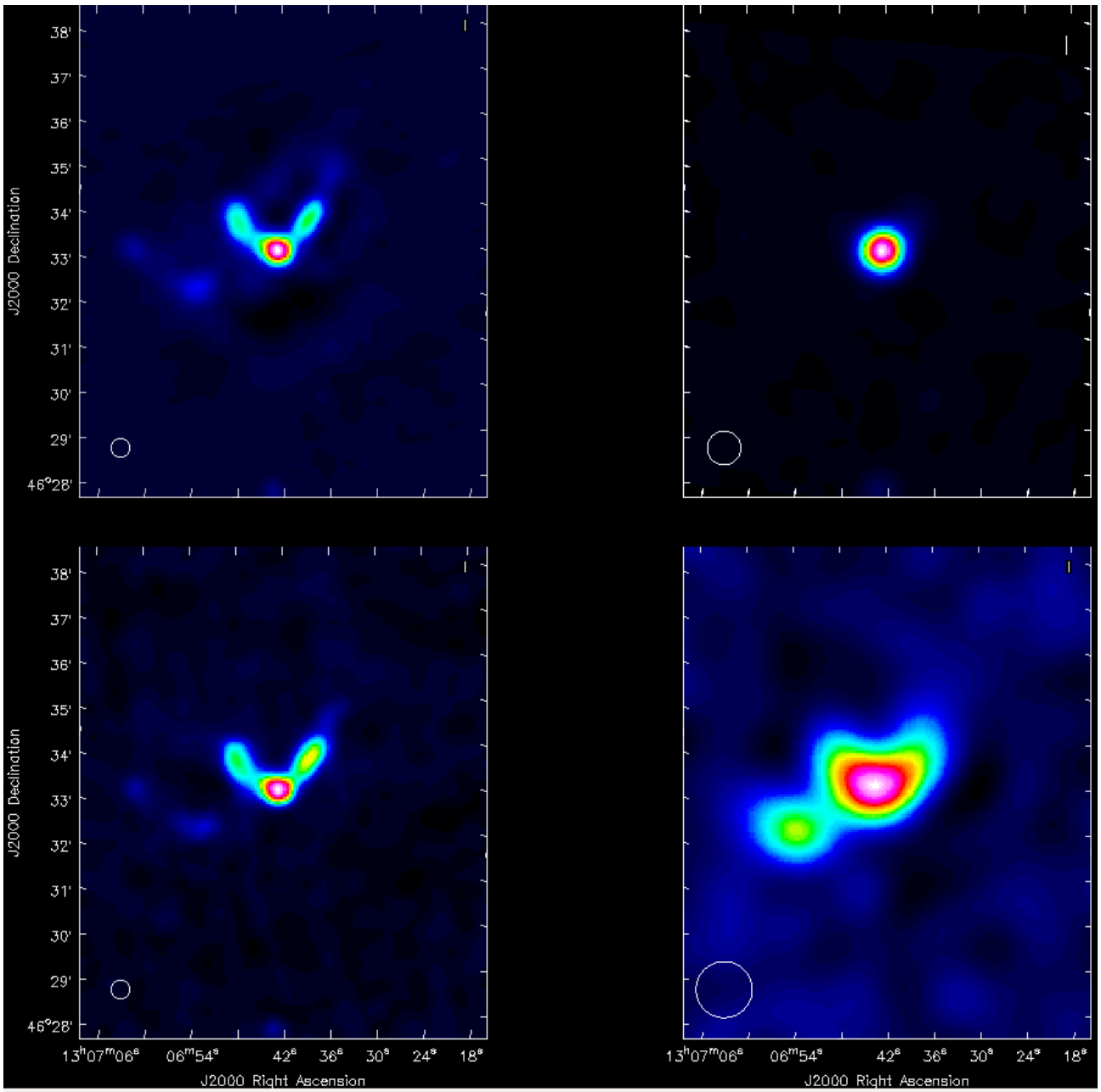

Figure 4.5: Radio images obtained from the LoTSS Preliminary Data Release (top left), NVSS data archive (top right), TGSS Alternative Data Release (bottom left) and VLSSr Data Archive (bottom right)

- Table 4.2 shows the radio fluxes and spectral indices of the emission regions integrated over the LoTSS and TGSS beam sizes, which is $25'' \times 25''$ for both telescopes;
- Table 4.3 shows the radio fluxes and spectral indices of the emission regions integrated over the NVSS beam size, which is $45'' \times 45''$;
- Table 4.4 shows the radio fluxes and spectral indices of the emission region integrated over the VLLSr beam sizes, which is $75'' \times 75''$.

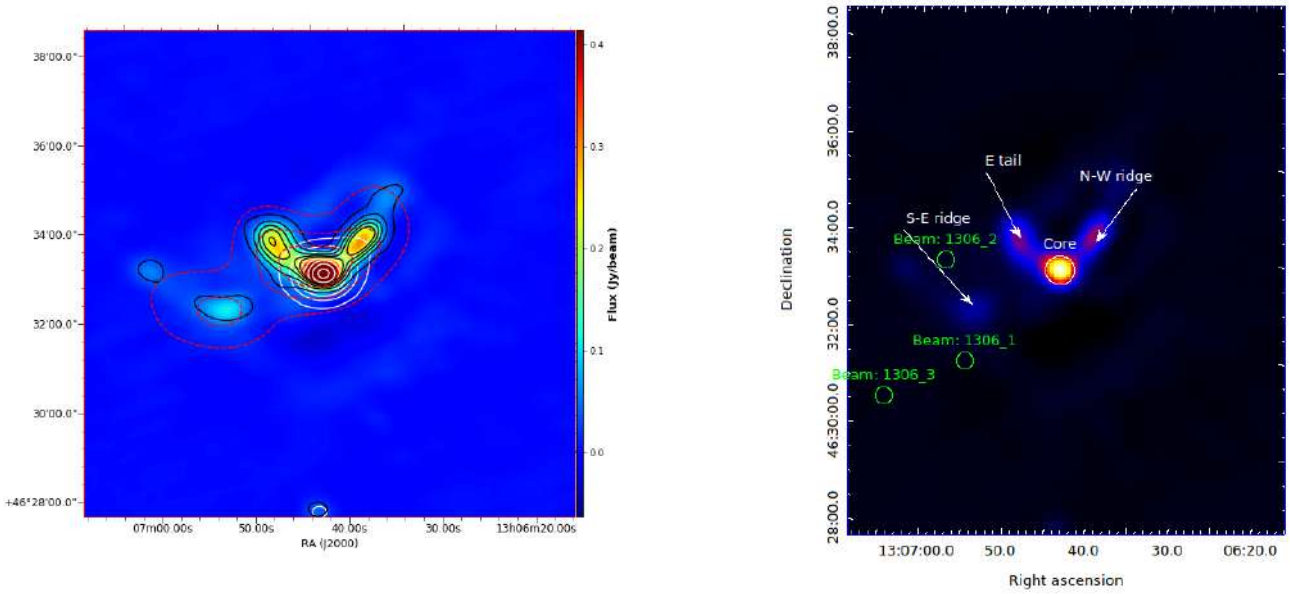

Figure 4.6: *Left:* LoTSS 125.3 MHz radio image with contours from the NVSS (white), TGSS (black) and VLLSr (red) images. *Right:* 125.3 MHz LOFAR radio image, the regions in white represent the regions originally observed by the GMRT radio halo survey as labeled on the GMRT survey (Venturi et al. 2008 and 2013), the green regions show the positions of the projected structures along the line of sight as observed by Ammons et al. (2013).

Region	R.A (J2000) hh mm ss	Dec (J2000) ° ′ ″	S_{LoTSS} mJy	S_{NVSS} mJy	S_{TGSS} mJy	S_{VLSSr} mJy	$\alpha^{1.4GHz}_{125.3MHz}$	$\alpha^{150MHz}_{125.3MHz}$
Core	13:06:45.7	46:33:31.8	447.12 ± 44.71	32.99 ± 3.30	458.59± 45.86	1 381.01± 208.5	-1.08±0.145	0.141 ±0.0373
E-tail	13:06:51.1	46:34:05.1	169.94 ± 17.00	1.02 ± 0.10	165.38 ± 16.54	1 381.01 ± 208.3	-2.12 ±0.138	-0.151±0.194
N-W ridge	13:06:41.9	46:34:17.8	177.46 ± 17.75	2.72 ± 0.27	214.91 ± 21.49	1 381.01± 208.4	-1.73 ±0.145	1.06±0.099
S-E ridge	13:06:55.6	46:32:31.9	68.99 ± 6.90	0.133 ±0.013	43.37 ± 4.34	1 381.01 ± 209.02	-2.59 ±0.139	-2.58±0.491

Table 4.2: Characteristics of the radio emissions found in A1682 integrated over a beam size $25'' \times 25''$. The VLSSr radio fluxes are upper limit values.

For all the tables, column (1) is the name of emission the region as labeled in Figure 4.6; column (2) and (3) provides the region's position as observed by the LOFAR telescope, this is also position where the circular shape of the beam was centered. Column (4), (5), (6) and (7) are the integrated fluxes of each region at 125.3 MHz, 1.4 GHz, 150 MHz and 73.8 MHz respectively. Column (8) is the spectral index between 125.3 MHz and 1.4 GHz and column (9) is the spectral index between 125.3 MHz and 150 MHz. All the flux density values for VLSSr were found to be less than the telescopes upper limit flux density, $3S_\sigma$. We replaced these values with $3S_\sigma$ at that beam size.

All the spectral index values, α, for each region are calculated using the form $S \propto v^\alpha$.

The flux density tables show that the core of the radio galaxy is the most powerful and brightest region (in the radio band) of A1682, followed by the N-W ridge and E-tail. The core also shows

Region	R.A (J2000) hh mm ss	Dec (J2000) ° ′ ″	S_{LoTSS} mJy	S_{NVSS} mJy	S_{TGSS} mJy	S_{VLSSr} mJy	$\alpha_{125.3MHz}^{1.4GHz}$	$\alpha_{125.3MHz}^{150MHz}$
Core	13:06:45.7	46:33:31.8	951.12 ± 95.11	87.67 ± 8.77	964.75± 96.48	1 694.88± 243.8	-0.988±0.133	0.079±0.021
E-tail	13:06:51.1	46:34:05.1	440.04 ± 44.01	3.71 ± 0.37	431.14 ± 43.11	1 694.88± 243.8	-1.98 ±0.131	0.114±0.015
N-W ridge	13:06:41.9	46:34:17.8	419.69 ± 41.97	8.79 ± 0.88	517.67 ± 51.77	1 694.88± 243.8	-1.96 ±0.164	1.17±0.110
S-E ridge	13:06:55.6	46:32:31.9	167.36 ± 16.74	0.4007 ±0.040	92.095 ± 9.21	1 694.88± 243.8	-2.501 ±0.134	-3.319±0.632

Table 4.3: Characteristics of the radio emissions found in A1682 integrated over a beam size $45'' \times 45''$. The VLSSr radio fluxes are upper limit values.

Region	R.A (J2000) hh mm ss	Dec (J2000) ° ′ ″	S_{LoTSS} mJy	S_{NVSS} mJy	S_{TGSS} mJy	S_{VLSSr} mJy	$\alpha_{125.3MHz}^{1.4GHz}$	α_{125MHz}^{150MHz}
Core	13:06:45.7	46:33:31.8	1 411.07 ± 141.11	157.37 ± 15.74	1 383.10± 13.83	1 977.36± 316.38	-0.91±0.122	0.11±0.029
E-tail	13:06:51.1	46:34:05.1	771.39 ± 77.14	13.55 ± 1.36	740.36 ± 74.04	1 977.36± 316.38	-1.675 ±0.111	-0.228±0.029
N-W ridge	13:06:41.9	46:34:17.8	675.46 ± 67.55	29.11 ± 2.91	875.00 ± 87.50	1 977.36± 316.38	-1.30 ±0.109	1.44±0.136
S-E ridge	13:06:55.6	46:32:31.9	296.86 ± 29.69	1.18 ±0.12	149.98 ± 15.00	1 977.36± 316.38	-2.29 ±0.123	-3.79±0.7219

Table 4.4: Characteristics of the radio emissions found in A1682 integrated over a beam size $75'' \times 75''$. The VLSSr radio fluxes are upper limit values

a flat radio spectrum for α_{125MHz}^{150MHz} as expected. The values of the spectral indices at the LoTSS and TGSS frequencies show large fluctuations because the flux density values of each region are almost the same. This can be attributed to their nearly equivalent low frequencies and similar beam sizes.

A plot of the integrated spectra for all the prominent radio sources and the multi-frequency spectral energy distribution (SED) for the A1682 cluster is shown in Figure 4.7. The integrated spectra (left image) is obtained using flux values integrated over the LoTSS (or TGSS) beam. The values for the SED are obtained from the SSDC sky explorer online tool[2] but with the addition of the LoTSS and TGSS fluxes (of the core region) derived from this study. A closer look at the integrated spectra shows that the S-E ridge is very steep, with higher radio fluxes at the lower frequencies and lower radio fluxes at higher frequencies. The S-E ridge follows the power law rule, which is expected from synchrotron emissions. The SED also shows that the cluster is dominated by radio emission at lower frequencies and soft X-ray emission at higher frequencies.

Figure 4.8 shows the spectral index map and the spectral index error map obtained from the LoTSS and TGSS refined images at frequencies $v_1 = 150MHz$ and $v_2 = 125.3MHz$.

4.2.2 Energy density and magnetic fields

In order to understand the magnetic field strength associated with the emission regions in the cluster we use the radio data we have obtained thus far to estimate the magnetic field strength around these radio regions. We used the equipartition estimation which has been discussed in detail in previous chapters to estimate the minimum energy density and consequently the magnetic fields of each radio region at 125.3 MHz. To do this we first calculated the surface brightness of each region at redshift $z = 0.226$, and a beam area of $\theta^2 = 508{,}844$ arcsec^2. We also calculated the radio power of each region at 125.3 MHz to help us throw some light on the properties of the N-W and S-E regions.

[2]https://tools.asdc.asi.it/

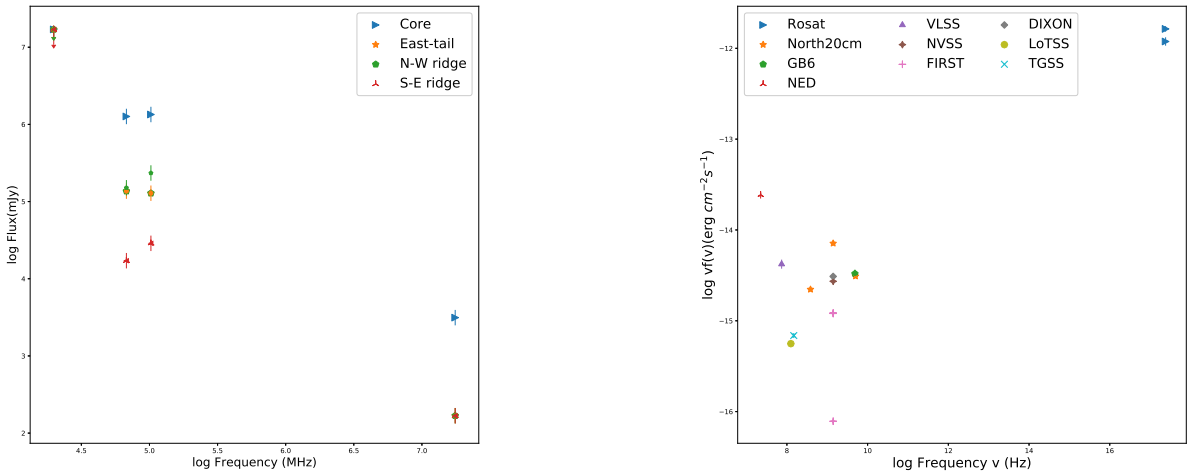

Figure 4.7: *Left:* A graph showing the integrated spectra of the radio sources observed in the cluster at different radio frequencies *Right:* The multi-frequency SED for the the A1682 cluster obtained from ASDC Sky Explorer and an additional two points (LoTSS and TGSS) obtained from this study

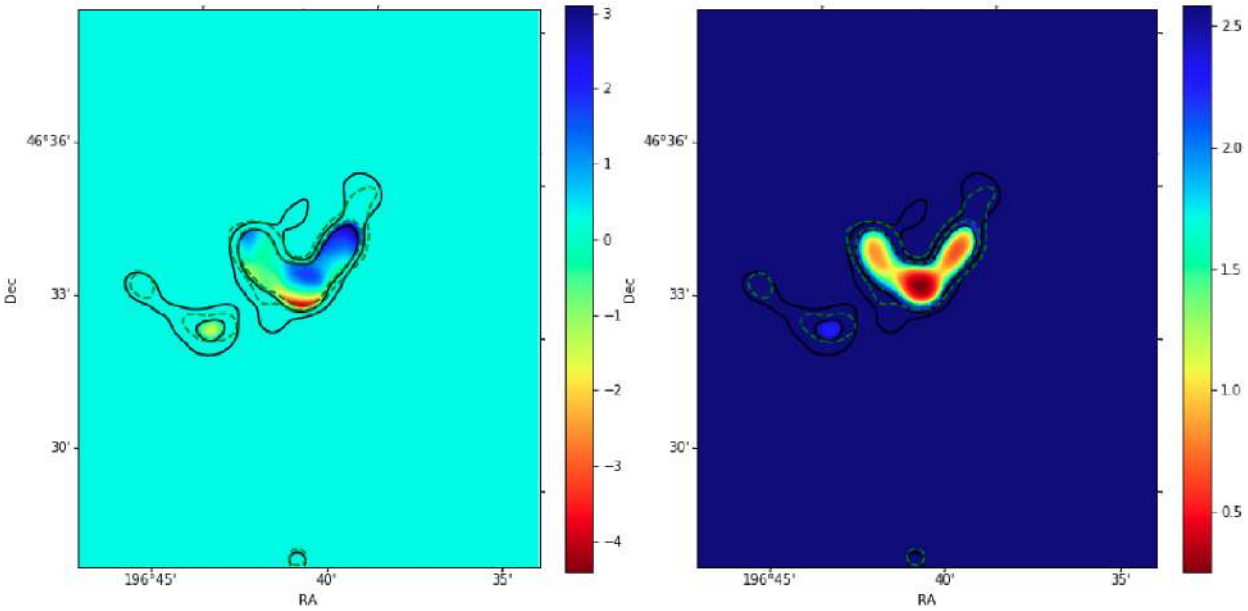

Figure 4.8: *Left:* The spectral index map of the A1682 cluster between 125.3 MHz and 150 MHz with a resolution of $25'' \times 25''$ and pa $= 22.5°$, overlaid with radio contours from TGSS and LOTSS images. The TGSS contours(green-dashed) are from 0.0288 to 0.1mJy/b in intervals of 2×0.0272mJy/b and the LoTSS contours (black) are from 0.0272 to 0.1mJy/b intervals of 2×0.0272mJy/b. *Right* The spectral index error map of the cluster with the same characteristics as the image on the left

Region	$I_{125.3MHz}$ $(mJyarcsec^{-2})$	$P_{125.3MHz}$ $(\times 10^{22} W/Hz)$	U_{min} $(\times 10^{-13} ergcm^{-3})$	B_{eq} (μG)
Core	0.879 ±0.066	0.382 ±0.045	1.060 ±0.136	1.068±0.198
E-tail	0.334 ±0.022	0.145 ±0.0214	0.420 ±0.055	0.673±0.139
N-W ridge	0.349 ±0.026	0.151 ±0.023	0.397±0.052	0.654±0.135
S-E ridge	0.136 ±0.0089	0.0589 ±0.0506	0.476±0.15	0.716±0.237

Table 4.5: Properties of the the discrete radio regions at 125.3 MHz. column 1: Region name, column 2: The peak surface brightness, column 3: The radio power, column 4: The minimum energy density at $z = 0.226$, Col. 5: The corresponding equipartition magnetic field.

Table 4.5 shows the surface brightness, radio power, minimum energy density ($u_{\rm min}$[erg/cm^3]) and magnetic field ($B_{\rm eq}[\mu$G]) of the discrete regions of the A1682 cluster.
The core region has the highest brightness, radio power, energy density and magnetic field strength values compared to the other radio emission regions, this is expected since the AGN is the most powerful and brightest radio source in the cluster. The values obtained for the magnetic fields in the core, E-tail and N-W ridge are comparable with magnetic field strengths of AGNs and their jets.

4.3 X-ray analysis

A1682 is known for its high X-ray luminosity and its ongoing merger and it would be interesting to find out if this has any relationship to the observed radio emission in the galaxy cluster. X-rays are from thermal gas and radio emission are from non-thermal electrons. However, cluster mergers (and derived shocks and/or turbulences) can be the link between the two emissions, by heating the gas and accelerating the non-thermal particles and it is important to check if radio and X-rays images are related each other to test this possibility. This will tell us if the diffuse emission is related to the ongoing cluster merger.

Figure 4.9 shows the X-ray emission of the cluster as observed by the Chandra survey, ACIS-I instrument. The image used (obs. ID. 11725) had an exposure time $\sim$ 20ks.
The X-ray image also shows an interesting and yet complex feature of the galaxy cluster. The cluster appears to have one X-ray source, which does not show any obvious relationship with the dominant radio source nor the diffuse radio emissions. The morphology of the X-ray emission is different from the morphologies of all the radio emissions and none of the radio emitting sources and diffuse radio regions are incident with the X-ray source of the cluster, although the X-ray emission does overlap marginally with the radio emission in some areas. The observations also show that the AGN has no (or very little) X-ray emission. We also observe two smaller X-ray emission hotspots which are very close to each other. The hotspots are close to the core of the dominant radiogalaxy but their emission is not extended. The S-E ridge also does not have any X-ray counterpart and is positioned in an area with low levels of X-ray radiation i.e., at the boundary of the X-ray emission as usually observed in radio relics.
In summary, the comparison of the X-ray observation with radio observations shows the highly disturbed gas distribution of the galaxy cluster, with different morphologies between the thermal and non-thermal gas. The X-ray emission spreads over a region of $\sim 880kpc$ in the cluster, it is highly likely that the difference of morphologies results from the ongoing cluster merger, this is

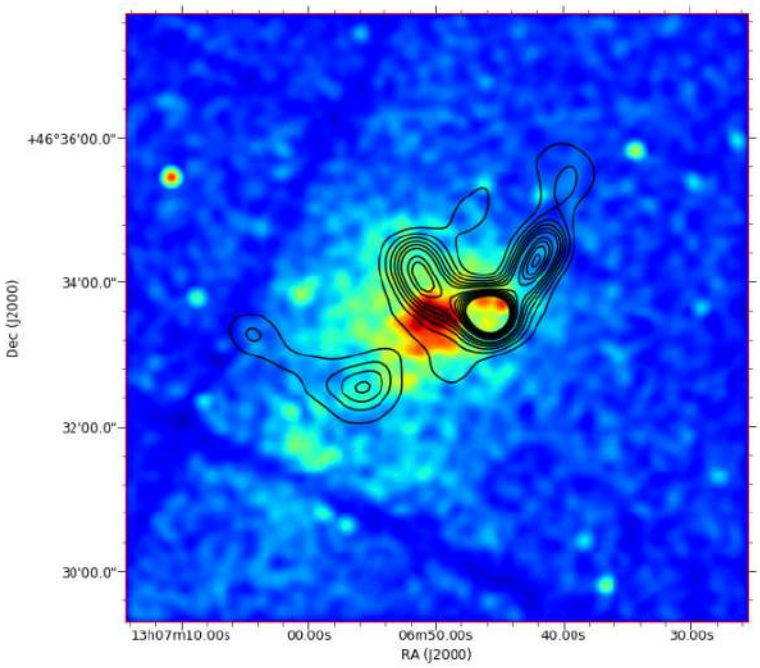

Figure 4.9: LoTSS 125.3 MHz radio contours of the A1682 cluster superimposed on the X-ray Chandra ACIS-I archive exposure map in the 0.2 - 5.0 keV energy band. The X-ray image was smoothed with a Gaussian kernel at $\sigma = 2$ pixels. The radio contours are from 0.0272 to 0.4 mJy/b in multiples of 0.0272 mJy/b

consistent with the observation of diffuse radio emission appearing all over the galaxy cluster (the candidate radio halo).

4.4 Infared and optical analysis

After studying the radio and X-ray emissions of A1682 we are interested in finding all the different sources responsible for the extended X-ray and radio emission in the cluster. We do this by firstly trying to identify their optical and infrared counterparts if they have any.

Figure 4.10 shows the RGB WISE infrared image of the A1682 cluster and Figure 4.11 shows the Hubble high resolution image of the cluster in the optical band. The IR image shows us the population of all present IR sources in the cluster, to help us identify if there are any sources visible in the IR band that can be associated to the S-E ridge and N-W tail. From these IR observations there seems to be no other radio galaxy situated next to the central AGN which can be associated to the N-W ridge and a further investigation around the position of the central AGN also shows no evidence of another active radio galaxy which might be positioned directly behind it at this cluster as hypothesized by Venturi et al. (2008). From the IR observations we can also see that the S-E ridge lacks and immediate IR counterpart. We found no sources in the IR band large enough to emit low surface brightness radio emission of this magnitude.

From the IR and optical images we are able see two sources located at the centers of the X-ray

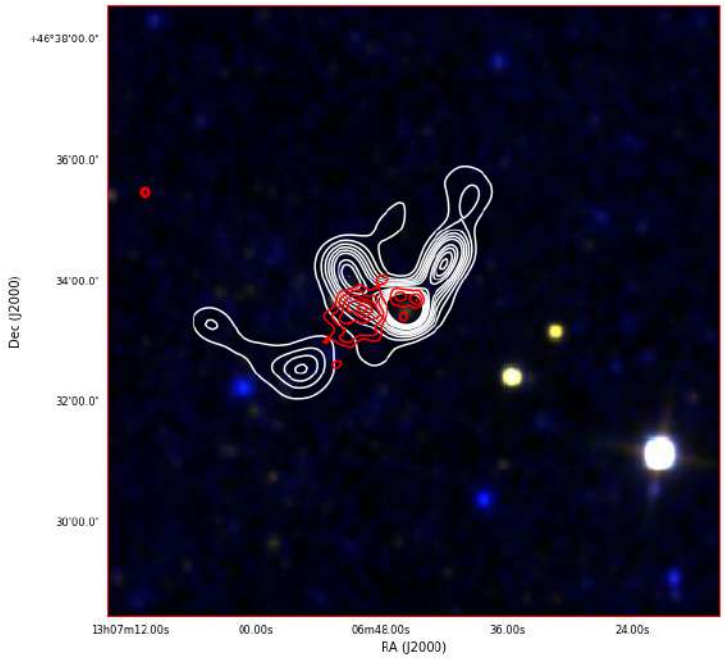

Figure 4.10: The WISE RGB image of the A1682 cluster overlaid with LoTSS radio and Chandra X-ray contours to show the position and extent of the diffuse emissions in the cluster. The radio contours are shown in white and are the same as previous image while the X-ray contours are shown in red.

and radio emissions, both these sources are luminous in the WISE RGB image and appear as point sources in the optical band. The X-ray emission centers around an elliptical galaxy with a confirmed spectroscopic redshift at $z = 0.232$, this galaxy is classified as the X-ray source 1RXSJ136053.3+463313 by the ROSAT All-Sky Survey (RASS) X-ray Catalogue. The X-ray source and AGN are positioned next to one another and are surrounded by bright stars and other cluster galaxies which can be identified on the SDSS optical telescope. The X-ray source 1RXSJ136053.3+463313 seems to be the central and dominant galaxy of the cluster and is situated about $44.8''$ ($\sim$ 167 kpc) from the radiogalaxy. A further analysis of the cluster in the optical band using Simbad [3] and SDSS shows that this cluster appears to be very rich in the optical band with a concentration of more galaxies about 451 kpc east of the two bright galaxies. Armed with this information and excluding all the unidentified bodies in the cluster we find that this cluster is a richness class II ($\sim$ 90 galaxies) in Abell richness classification and type II in the Bautz-Morgan classification.
The core of the radio galaxy is associated with a bright optical galaxy in the SDSS DR-13 with spectroscopic confirmation of its redshift at $z = 0.21835$ and a red magnitude of r=16.50 (SDSS). The redshift of the radio galaxy is different from the cluster's redshift, this can indicate that the galaxy is moving through the cluster along the line pf sight. This galaxy is also associated to a QORG (see Flesch and Hardcastle (2004) for the catalogue classification) at $0.7''$ distance from the galaxy position. This object is identified with the source A1304+4649A in the NASA/IPAC Extragalactic Database (NED).

[3]http://simbad.u-strasbg.fr/simbad

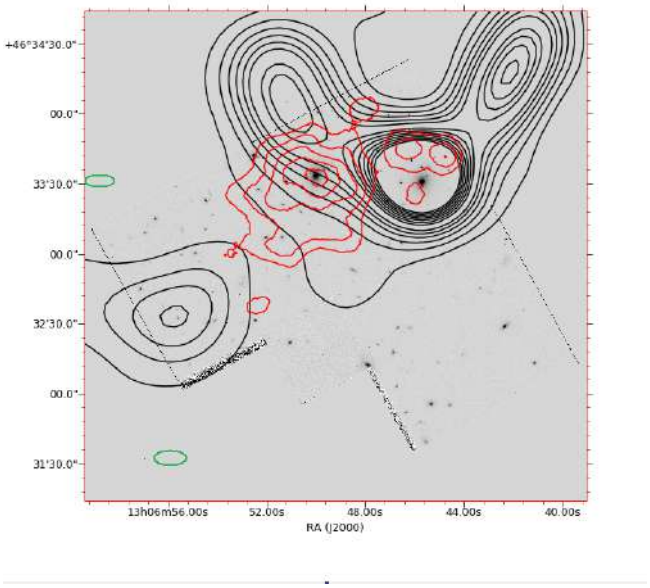

Figure 4.11: The Hubble high resolution optical image of the A1682 cluster overlaid with LoTSS radio (black) and Chandra X-ray (red) contours with the same properties. The position of the observed projected structures are shown by the green circles; the third arc is left out as it is an outlier.

The multi-frequency SED of the core of this radiogalaxy is dominated by non-thermal component at radio frequencies with a typical galaxy SED at infrared and optical frequencies. Figure 4.12 shows the multi-frequency SED of the QORG obtained from the SSDC sky explorer with an addition of the TGSS and LOTSS data as obtained from this study and the right image shows the spectrum of A1304+4949A. The spectroscopy of the QORG shows that it is a dominant elliptical radio galaxy.

The N-W ridge and E-tail both appear to continuously depart from the QORG, there is no evidence of another optical counterpart which can be associated with the central extended radio emissions. This leads us to conclude that both the E-tail and N-W ridge are the radio jets resulting from the QORG and not from another radio source. Their unusual bended structure is a result of the distortion in motion caused by the density of the ICM and rapid motions of the AGN. We found the angle between the two jets to be $\sim 100°$, thus leading us to conclude that the galaxy is an FRII WAT radiogalaxy, moving rapidly through the cluster in a downwards motion.
The Hubble optical image in Figure 4.11 does not show any optical counterpart that can be associated with the large S-E radio emission. We also did not find any evidence of a remnant radio galaxy in this region which might have been responsible for the emission. Due to the high resolutions of the Hubble telescope we are able to distinctly see the sources of the large thermal and non-thermal emissions in the cluster but the telescope can not cover a large area so we can only see a smaller portion of the cluster than we would've liked to. As seen on the optical image the radio contours of the S-E ridge are centered around small and random galactic objects, these objects are not known to be radio emitting sources and so their radio emission would be insignificantly smaller compared to the S-E emission. The lack of optical, infrared

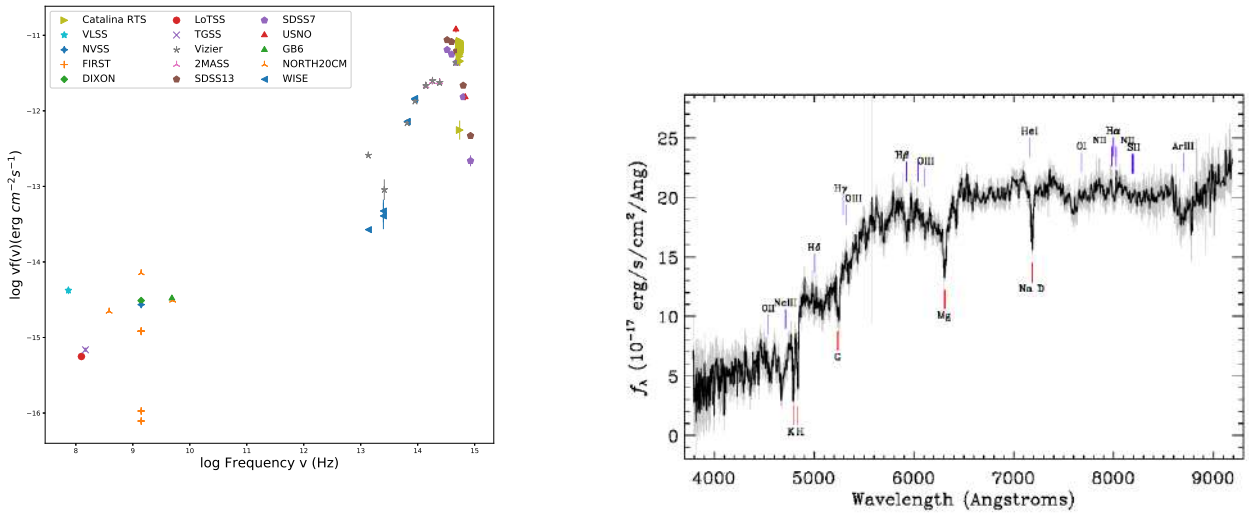

Figure 4.12: *Left:* The multi-frequency SED for the QORG from obtained from the SSDC Sky Explorer and an addition of two points (LoTSS and TGSS) obtained from this study. *Right:* The spectroscopy of the radio galaxy source A1304+4649.

and X-ray counterparts for the S-E ridge suggests that the optical redshift of the source might be higher. A higher redshift of the optical counterpart for this radio source may imply that the source is positioned behind the A1682 cluster and we are able to detect its radio emission due to the gravitational lensing effect.

4.5 Weak lensing and sub-millimeter observations

Previous studies have shown that A1682 is a weak lensing cluster, we now exploit this observation to check if the S-E emission can be a result of a weak lensing background structure. As much as strong lensing allows us to constrain the projected mass distribution of the cluster, weak lensing allows us to obtain shear maps which can be inverted to obtain a two dimensional lensing mass distribution of galaxy clusters. We use the lensing mass distribution constructed by Dahle et al. (2002) (figure 4.4) and compare it to the radio emission found in the S-E regions of the cluster.

Figure 4.13 shows the lensing mass distribution map overlaid with the radio contours of the S-E ridge, we also show the positions of the dark matter halos calculated by Ammons et al. (2013). We find that the lensing mass map is very close to the S-E emission's position. We also see that the two central dark matter halo masses are located within the lensing mass map and are positioned just outside the S-E ridge's radio contours. Another spectacular finding is that the lensing mass distribution has a morphology similar to that of the S-E ridge.
Since gravitation lensing can increases the size of the lensed structure but conserve its surface brightness, it is expected for the lensing mass to be have a larger size than the area covered by the radio emission. This could explain the small appearance of the S-E ridge compared to the size of the lensing mass distribution.

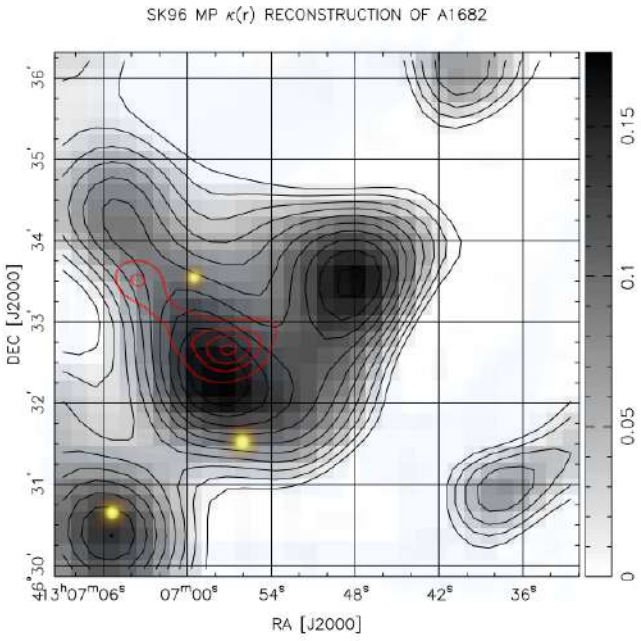

Figure 4.13: The radio contours of the candidate relic (in red) are superposed to the lensing mass distribution of A1682 from Dahle et al (2002). The bright spots represent the position of the observed arcs from Ammons et al (2013).

Figure 4.14 shows the Planck sub-mm 143 GHz, HFI CMB-subtracted map of the cluster, overlaid with the 125.3 MHz radio contours of the galaxy cluster. The sub-mm shows that the cluster is situated in a dense region where we would expect the highest concentration of dark matter which contributes to the gravitational collapse of matter. In such regions we could expect massive dark matter haloes interacting with baryonic matter via gravity and producing strong gravitational effects on matter along their line of sight. This strong gravitational interaction with baryonic matter would then favor gravitational lensing of large cosmological structure (i.e., galaxies) and CMB photons in the cluster. This also explains the size of the massive and large halo masses shown in table 4.1 as calculated by Ammons et al. (2013). We see that the high density of the gas in the cluster does favor the existence of massive dark matter halos (1306_1 and consequently 1306_2) located next to the S-E ridge. However, as much as this dense region favors the observation of gravitational lensing in the southern regions of the cluster it also favors the self-annihilation or decay of WIMPS inside the large dark matter haloes into observable products. In the following section we explore the consequences of the latter scenario.

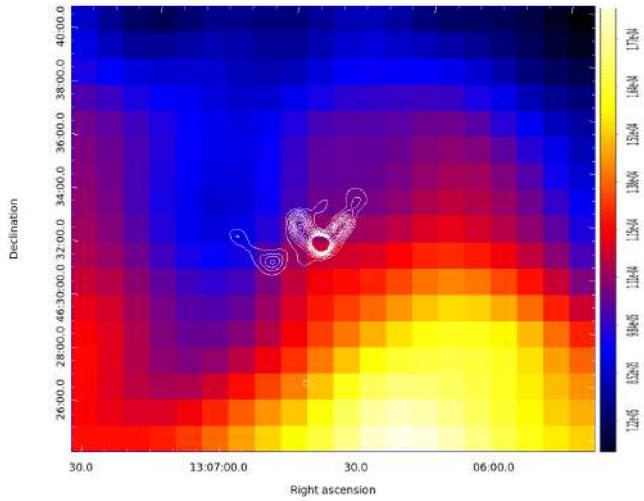

Figure 4.14: Planck 143GHz HFI CMB-subtracted image of a region containing the A1682 cluster to visualize the density of matter in the cluster

4.6 Annihilation of WIMPs in A1682

Since the peak of the S-E ridge is located close to the main halo mass in the cluster region (the halo 1306_1 in Ammons et al. (2013)), we test the possibility that the radio emission of the S-E ridge can be due to the annihilation of Dark Matter (DM) particles. We follow the approach presented in Colafrancesco et al. (2006), where the production rate of electrons/positrons and gamma rays is given by:

$$Q_i(E,\vec{r}) = \mathcal{B}\langle\sigma v\rangle\Sigma_f \frac{dN_i^f}{dE} B_f \mathcal{N}_\chi(\vec{r}), \tag{4.1}$$

where i is the index referring to the output electrons/positrons or photons, $\mathcal{B}$ is a boosting factor due to DM substructures (e.g., Pieri, Lavalle, Bertone, and Branchini (2011)), $\langle\sigma v\rangle$ is the thermally-averaged neutralino annihilation cross-section, the index f refers to the annihilation final states with branching ratios B_f, and $\mathcal{N}_\chi(\vec{r}) = (\rho(\vec{r}))^2/(2M_\chi^2)$ is the neutralino pair density. The production spectra dN_i^f/dE are calculated using the DarkSusy package (Gondolo et al., 2004).
The electrons/positrons are subject to the effects of energy losses and to the diffusion, according to the diffusion equation:

$$\frac{\partial}{\partial t}\frac{dn_e}{dE} = \nabla\left(D(E,\vec{r})\nabla\frac{dn_e}{dE}\right) + \frac{\partial}{\partial E}\left((b(E,\vec{r})\frac{dn_e}{dE}\right)) + Q_e(E,\vec{r}), \tag{4.2}$$

where dn_e/dE represents the spectrum of the electron, the coefficient $D(E,\vec{r})$ represents the spatial diffusion as a function of energy and the radial distribution, $b(E,\vec{r})$ represents the electron's energy-loss function and $Q_e(E,\vec{r})$ is the electron source function. A general solution of this equation, making use of the Green function, is presented in Colafrancesco et al. (2006).

We model the DM distribution in the halo 1306_1 following the procedure described in Bullock et al. (2001) and Colafrancesco, Marchegiani, and Beck (2015) that, for a halo mass of $2.0\times10^{15}M_\odot$,

provides a spherical symmetric Navarro Frenk White profile

$$\rho(r) = \frac{\rho_s}{(r/r_s)(1+r/r_s)^2}, \tag{4.3}$$

with a central density of $\rho_s = 4.2 \times 10^3 \rho_c$, where ρ_c is the critical density of the Universe, and $r_s = 680$ kpc.

We calculate the equilibrium distribution of the electrons for the two DM models that have been found to provide a best fitting to the spectrum of the radio halo of the Coma cluster (Marchegiani & Colafrancesco, 2016): *i)* neutralino with mass $M_\chi = 9$ GeV, composition $\tau^+\tau^-$, and $\mathcal{B} \times \langle \sigma v \rangle = 6 \times 10^{-25}$ cm^3 s^{-1}; *ii)* neutralino with mass $M_\chi = 43$ GeV, composition $b\bar{b}$, and $\mathcal{B} \times \langle \sigma v \rangle = 4 \times 10^{-24}$ cm^3 s^{-1}.

We calculate the radio emission produced by the electrons by varying the value of the magnetic field in the halo; as noted by Colafrancesco et al. (2006), the resulting spectral shape depends on the value of the magnetic field because of the spectral curvature of the electrons spectrum. By comparing the resulting spectrum with the spectrum of the S-E ridge (see Table 4.2), it is possible to obtain an estimate of the magnetic field value that allows to produce a spectral shape similar to the observed one. The best fit values of the magnetic field are $B = 0.55$ μG for the 9 GeV model, and $B = 0.06$ μG for the 43 GeV model. By using the normalizations of the electrons spectra provided by the product $\mathcal{B} \times \langle \sigma v \rangle$ as found for the Coma cluster (Marchegiani & Colafrancesco, 2016), we find that the intensity of the flux produced by these models needs to be multiplied by another factor of the order of 12 for the 9 GeV model, and of the order of 2500 for the 43 GeV model. In Figure 4.15 we show the radio spectrum obtained in these cases. The magnetic field found in the 9 GeV case is reasonable, considering that the DM peak is located quite far from the X-ray peaks, and therefore a magnetic field value smaller, but still comparable with the values of a few μG usually found in the centre of galaxy clusters (e.g., Govoni and Feretti (2004)). It is also compatible with the value of the magnetic field in the same region obtained under the equipartition assumption in Table 4.5. The magnetic field found in the 43 GeV case instead appears to be too low for typical galaxy clusters.
The presence of the additional multiplicative factor can be interpreted as due to the effect of the adiabatic compression of the electrons produced by a shock, that is necessary to explain the elongated shape of the S-E ridge (Enßlin, 2001). As found by Colafrancesco, Marchegiani, and Paulo (2017), the effect of the adiabatic compression is to amplify the radio emission by a factor depending on the Mach number, $\mathcal{M}$, of the shock and the spectral index of the electrons. By applying the eq.(17) in Colafrancesco et al. (2017) for an electron spectral index of $s = 6.2$, corresponding to the spectral index $\alpha = 2.6$ found in the S-E ridge, we find that a multiplicative factor of 12, as required by the 9 GeV model, requires a weak shock with $\mathcal{M} \sim 1.4$, whereas a multiplicative factor of 2500, as required by the 43 GeV model, requires a stronger shock with $\mathcal{M} \sim 3.2$. The S-E ridge appears to be close to the edge of the main X-ray halo of the cluster (see Figure 4.9), and therefore it is possible that a shock is present in this region. However, the relatively small size and power of the S-E ridge compared to what is usually observed in radio relics that can have a similar origin (Colafrancesco et al., 2017), suggests that a shock, if present, should be quite weak, indicating again the 9 GeV model as the one favored.
We also test these models by calculating the Inverse Compton Scattering (ICS) on the CMB produced in the X-rays by the same electrons, and the gamma ray emission produced in DM annihilation. As shown in Figure 4.16, the IC scattering emission for the 9 GeV model is

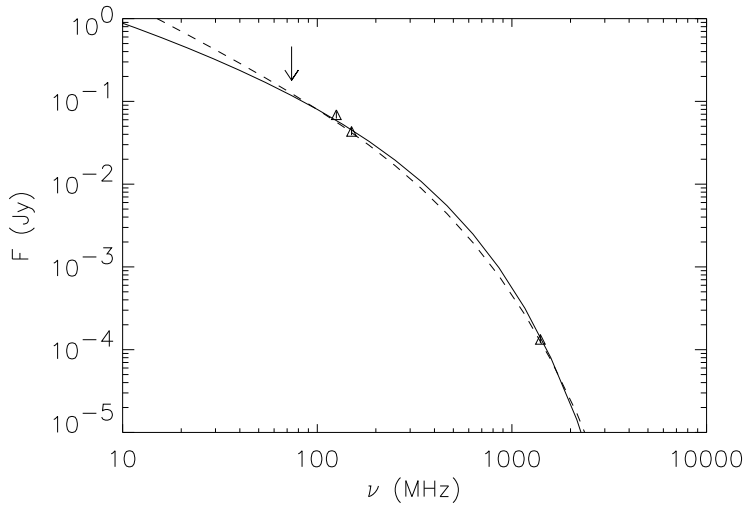

Figure 4.15: Radio spectrum produced by annihilation of dark matter compared with the data points of the S-E ridge for: *i)* a neutralino model with mass $M_\chi = 9$ GeV, composition $\tau^+\tau^-$, $\mathcal{B} \times \langle\sigma v\rangle = 6 \times 10^{-25}$ cm^3 s^{-1}, and an additional multiplicative factor of 12 (solid line); *ii)* a neutralino model with mass $M_\chi = 43$ GeV, composition $b\bar{b}$, $\mathcal{B} \times \langle\sigma v\rangle = 4 \times 10^{-24}$ cm^3 s^{-1}, and an additional multiplicative factor of 2500 (dashed line); data are from Table 4.2.

dominant compared to the thermal emission of the cluster only at energies $E > 50$ keV, and is below the sensitivity limit expected for Astro-H at all the energies; the ICS emission in the 43 GeV model is instead comparable to the thermal emission of the cluster even at low energies, and is dominant at $E > 20$ keV, where it can be detected by Astro-H until 70 keV. The observations in this spectral band therefore appear to be suitable to distinguish between these two models.

We also calculate the gamma ray emission produced by DM annihilation for the same DM models; in this case, since the DM and the produced photons are not affected by the shock compression, we don't multiply the resulting emission by the additional multiplicative factor applied to the electrons. Since no upper limits are available for this specific cluster, in Figure 4.17 we show the calculated gamma ray emission compared with the Fermi-LAT expected sensitivity limit for 10 yrs of operation time (from Funk & Hinton 2013). In both cases the expected emission is below the sensitivity of Fermi-LAT, as confirmed by the value of the integrated flux $F(> 100$ MeV), that is 8.5×10^{-13} cm^{-2} s^{-1} for the 9 GeV model, and 6.3×10^{-11} cm^{-2} s^{-1} for the 43 GeV model, whereas the typical values of gamma ray upper limits in galaxy clusters in this band are of the order of 10^{-9} cm^{-2} s^{-1} (Ackermann et al., 2011, 2014) (Ackermann et al., 2014) (Ackermann et al. 2010; 2014). We therefore don't expect the gamma ray emission produced by DM annihilation can be observed in this cluster.

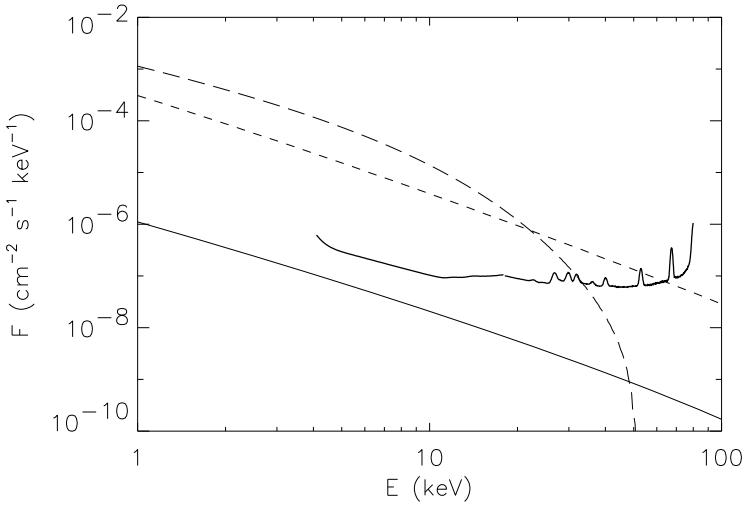

Figure 4.16: X-ray emission by ICS produced in the DM models with mass 9 GeV (solid line) and mass 43 GeV (dashed line), compared with the thermal emission of the cluster, calculated assuming a temperature of 7 keV and a bolometric luminosity of 1.53×10^{45} erg s^{-1} (Reichert et al. 2011; long-dashed line), and the sensitivity of Astro-H HXI for 100 ks of time integration (from http://astro-h.isas.jaxa.jp/researchers/sim/sensitivity.html; thick line). See caption of Figure4.15 for the details of the DM models.

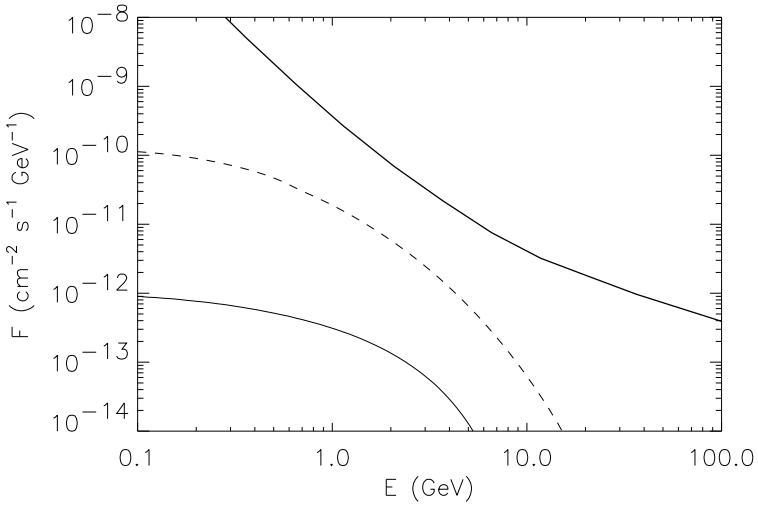

Figure 4.17: Gamma ray emission resulting from the annihilation of DM in the models with mass 9 GeV (solid line) and mass 43 GeV (dashed line), compared with the sensitivity of Fermi-LAT for 10 yrs of operation time (from Funk & Hinton 2013; thick line). See caption of Fig.4.15 for the details of the DM models.

5 Summary and Conclusions

The purpose of this research was to use multi-frequency observations to study the origin of the radio emission found in the A1682 galaxy cluster. Our primary interest was classifying the N-W and S-E ridges and their relationship with the radiogalaxy, ongoing merger and dark matter. We summarize the main results of our analysis as follows:

- Abell 1682 is an optically rich cluster, dominated by two central elliptical galaxies. It has richness class II in the Abell richness classification and type II cluster in the Bautz-Morgan classification.

- The galaxy cluster shows a difference in morphology and sizes in the distribution of thermal and non-thermal gas. The X-ray and the bulk of the radio emission originates from two dominant elliptical galaxies.Our analysis revealed that there is no relationship between the X-ray and radio emission in the cluster.

- The X-ray emission results from the central BCG associated with the source 1RXSJ136053.3+463313 in the RASS catalogue. The galaxy has a spectroscopic redshift $z = 0.232$ and is situated about 167 kpc north east of the dominant radio galaxy.

- A radio analysis of the cluster revealed that the bulk of the emission in the A1682 galaxy cluster originates from the dominant elliptical FRII radiogalaxy, associated with the source A1304+4649 in NED. The radiogalaxy has a spectroscopic redshift $z = 0.21835$.

- Due to the lack of X-ray, optical and IR counterparts or any other radiogalaxy at the cluster's redshift, we concluded that the N-W ridge is a radio jet ejected from the dominant radio galaxy. Its distorted morphology is due to the ram pressure exerted by the ICM gas. The angle in-between the jets from the radiogalaxy suggest that the cluster is moving at rapid motion in the downwards position of the cluster, making the AGN a WAT FRII type radiogalaxy.

- Our analysis of the S-E ridge showed that this emission is not related to the dominant radio galaxy or the BCG.

- The S-E ridge appears in both the GMRT and LOFAR, but is not a prominent feature on the VLSSr and NVSS radio images radio images. The emission doesn't show any relationship with the dominant elliptical galaxies, We also didn't find any relationship

of this emission to the ongoing cluster merger and the positive radio residuals spread all over the cluster. A further analysis of this emission does shows that the emission does not have any IR, X-ray and optical counterpart at the cluster's redshift. This suggests that the distance of this source might be higher (i.e., positioned behind A1682)

- A comparison of previous lensing studies of this cluster with the S-E emission reveals that the S-E ridge is positioned in-between two massive dark matter halos of magnitude $10^{14-15} M_{\odot}$, the emission is also coincident with the largest lensing mass distribution in the cluster. This analysis also showed us that lensing mass and the S-E ridge are along the same line of sight.

- Since there are two large dark matter haloes situated around the S-E emission, we studied the possibility of this synchrotron emission resulting from the annihilation of a WIMP inside the halo. We found that this is possible for a model with a super-symmetric neutralino, χ of mass, M_{χ} =9GeV, with a $\tau^{+}\tau^{-}$ composition at a magnetic field of $B = 0.55\mu G$ when using the largest halo mass. Although the model needs a large multiplicative factor to produce the radio fluxes it explains the elongated structure of the S-E ridge as the effect of the compression produced by a weak shock front (not detected until now) and it's steepness at higher frequencies.

- We then concluded that the S-E ridge either results from a weak gravitationally lensing radiogalaxy positioned at a higher redshift or is a product of the annihilation of a spherical dark matter halo situated at the peripheral regions of the cluster.

- At this point, no conclusion can be made on the origin of the candidate radio halo and its relationship with the ongoing merger.

5.1 Future prospects

This research presents the beginning steps on the study of clusters using multi-frequency observations, gravitational lensing and the dark matter annihilation to understand the origin of diffuse radio emission in galaxy cluster. In the future we would like to:

- Use the X-ray emission data of the cluster to study the temperatures and the density of the ICM and derive information on the connection between the ongoing merger and candidate radio halo.

- Study the level of comptonization of the gas in the cluster (SZ effect) using the cluster's Planck map and its relationship to the X-ray emission

- Investigate the motion of the dominant radio galaxy and its effect on the distribution of the thermal and non-thermal gas in the cluster.

- We would like to investigate more clusters where the data from both the diffuse radio emission and gravitational lensing is available to study the contribution of dark matter annihilation in radio halos and relics.

6 References

References

Abdo, A., Ackermann, M., Ajello, M., Baldini, L., Ballet, J., Barbiellini, G., ... others (2010). Constraints on cosmological dark matter annihilation from the fermi-lat isotropic diffuse gamma-ray measurement. *Journal of Cosmology and Astroparticle Physics*, *2010*(04), 014.

Abell, G. O. (1958). The distribution of rich clusters of galaxies. *The Astrophysical Journal Supplement Series*, *3*, 211.

Abell, G. O. (1965). Clustering of galaxies. *Annual Review of Astronomy and Astrophysics*, *3*(1), 1–22.

Ackermann, M., Ajello, M., Albert, A., Allafort, A., Atwood, W., Baldini, L., ... others (2014). Search for cosmic-ray-induced gamma-ray emission in galaxy clusters. *The Astrophysical Journal*, *787*(1), 18.

Ackermann, M., Ajello, M., Albert, A., Baldini, L., Barbiellini, G., Bechtol, K., ... others (2012). Fermi lat search for dark matter in gamma-ray lines and the inclusive photon spectrum. *Physical Review D*, *86*(2), 022002.

Ackermann, M., Ajello, M., Albert, A. t., Atwood, W., Baldini, L., Ballet, J., ... others (2011). Constraining dark matter models from a combined analysis of milky way satellites with the fermi large area telescope. *Physical Review Letters*, *107*(24), 241302.

Ackermann, M., Ajello, M., Allafort, A., Baldini, L., Ballet, J., Barbiellini, G., ... others (2010). Constraints on dark matter annihilation in clusters of galaxies with the fermi large area telescope. *Journal of Cosmology and Astroparticle Physics*, *2010*(05), 025.

Ammons, S. M., Wong, K. C., Zabludoff, A. I., & Keeton, C. R. (2013). Mapping compound cosmic telescopes containing multiple projected cluster-scale halos. *The Astrophysical Journal*, *781*(1), 2.

Arlen, T., Aune, T., Beilicke, M., Benbow, W., Bouvier, A., Buckley, J., ... others (2012). Constraints on cosmic rays, magnetic fields, and dark matter from gamma-ray observations of the coma cluster of galaxies with veritas and fermi. *The Astrophysical Journal*, *757*(2), 123.

Arnaud, M., Aghanim, N., Gastaud, R., Neumann, D., Lumb, D., Briel, U., ... others (2001). Xmm-newton observation of the coma galaxy cluster-the temperature structure in the central region. *Astronomy & Astrophysics*, *365*(1), L67–L73.

Bacchi, M., Feretti, L., Giovannini, G., & Govoni, F. (2003). Deep images of cluster radio halos. *Astronomy & Astrophysics*, *400*(2), 465–476.

Bahcall, N. A., & Fan, X. (1998). The most massive distant clusters: Determining Ω and $\sigma 8$. *The Astrophysical Journal*, *504*(1), 1.

Bautz, L., & Morgan, W. (1970). On the classification of the forms of clusters of galaxies. *The Astrophysical Journal*, *162*, L149.

Beck, G., & Colafrancesco, S. (2016). A multi-frequency analysis of dark matter annihilation interpretations of recent anti-particle and γ-ray excesses in cosmic structures. *Journal of Cosmology and Astroparticle Physics*, *2016*(05), 013.

Becker, W., Swartz, D. A., Pavlov, G. G., Elsner, R. F., Grindlay, J., Mignani, R., ... others (2003). Chandra x-ray observatory observations of the globular cluster m28 and its millisecond pulsar psr b1821–24. *The Astrophysical Journal*, *594*(2), 798.

Bertone, G., Hooper, D., & Silk, J. (2005). Particle dark matter: Evidence, candidates and constraints. *Physics Reports*, *405*(5), 279–390.

Biermann, L. (1950). L. biermann, z. naturforsch. a 5, 65 (1950). *Z. Naturforsch. A*, *5*, 65.

Birkinshaw, M. (1999). The sunyaev–zel'dovich effect. *Physics Reports*, *310*(2-3), 97–195.

Bliton, M., Rizza, E., Burns, J., Owen, F., & Ledlow, M. (1998). Cluster-subcluster mergers and the formation of narrow-angle tailed radio sources. *Monthly Notices of the Royal Astronomical Society*, *301*(3), 609–625.

Bonafede, A., Feretti, L., Giovannini, G., Govoni, F., Murgia, M., Taylor, G., ... Pihlström, Y. (2009). Revealing the magnetic field in a distant galaxy cluster: discovery of the complex radio emission from macs j0717. 5+ 3745. *Astronomy & Astrophysics*, *503*(3), 707–720.

Brunetti, G. (2002). Modelling the non-thermal emission from galaxy clusters. *arXiv preprint astro-ph/0208074*.

Brunetti, G., Cassano, R., Dolag, K., & Setti, G. (2009). On the evolution of giant radio halos and their connection with cluster mergers. *Astronomy & Astrophysics*, *507*(2), 661–669.

Brunetti, G., Setti, G., Feretti, L., & Giovannini, G. (2001). Particle injection and reacceleration in clusters of galaxies and the euv excess: the case of coma. *New Astronomy*, *6*(1), 1–15.

Bullock, J. S., Kolatt, T. S., Sigad, Y., Somerville, R. S., Kravtsov, A. V., Klypin, A. A., ... Dekel, A. (2001). Profiles of dark haloes: evolution, scatter and environment. *Monthly Notices of the Royal Astronomical Society*, *321*(3), 559–575.

Cantwell, T., Scaife, A., Oozeer, N., Wen, Z., & Han, J. (2016). A newly discovered radio halo in merging cluster macs j2243. 3-0935. *Monthly Notices of the Royal Astronomical Society*, *458*(2), 1803–1814.

Carilli, C., & Taylor, G. (2002). Cluster magnetic fields. *Annual Review of Astronomy and Astrophysics*, *40*(1), 319–348.

Carlstrom, J. E., Joy, M., & Grego, L. (1996). Interferometric imaging of the sunyaev-zeldovich effect at 30 ghz. *The Astrophysical Journal Letters*, *456*(2), L75.

Cassano, R., Brunetti, G., & Venturi, T. (2011). The connection between radio halos and cluster mergers and the statistical properties of the radio halo population. *Journal of Astrophysics and Astronomy*, *32*(4), 519–527.

Cavaliere, A., Gursky, H., & Tucker, W. (1971). Extragalactic x-ray sources and associations of galaxies. *Nature*, *231*(5303), 437.

Clowe, D., Bradač, M., Gonzalez, A. H., Markevitch, M., Randall, S. W., Jones, C., & Zaritsky, D. (2006). A direct empirical proof of the existence of dark matter. *The Astrophysical Journal Letters*, *648*(2), L109.

Clowe, D., Randall, S., & Markevitch, M. (2007). Catching a bullet: direct evidence for the existence of dark matter. *Nuclear Physics B-Proceedings Supplements*, *173*, 28–31.

Cohen, A., Lane, W., Cotton, W., Kassim, N., Lazio, T., Perley, R., ... Erickson, W. (2007). The vla low-frequency sky survey. *The Astronomical Journal*, *134*(3), 1245.

Colafrancesco, S. (2007). Beyond the standard lore of the sz effect. *New Astronomy Reviews*, *51*(3), 394–405.

Colafrancesco, S. (2010). Dark matter in modern cosmology. In *Aip conference proceedings* (Vol. 1206, pp. 5–26).

Colafrancesco, S., Marchegiani, P., & Beck, G. (2015). Evolution of dark matter halos and their radio emissions. *Journal of Cosmology and Astroparticle Physics*, *2015*(02), 032.

Colafrancesco, S., Marchegiani, P., & Buonanno, R. (2011a). Untangling the atmosphere of the bullet cluster with sunyaev-zel'dovich effect observations. *Astronomy & Astrophysics*, *527*, L1.

Colafrancesco, S., Marchegiani, P., & Paulo, C. (2017). The correlation between radio power and mach number for radio relics in galaxy clusters. *Monthly Notices of the Royal Astronomical Society*, *471*(4), 4747–4759.

Colafrancesco, S., & Mele, B. (2001). Neutralinos and the origin of radio halos in clusters of galaxies. *The Astrophysical Journal*, *562*(1), 24.

Colafrancesco, S., Profumo, S., & Ullio, P. (2006). Multi-frequency analysis of neutralino dark matter annihilations in the coma cluster. *Astronomy & Astrophysics*, *455*(1), 21–43.

Collaboration, P., et al. (2014). Planck 2013 results. xvi. cosmological parameters.

Condon, J. (1992). Radio emission from normal galaxies. *Annual review of astronomy and astrophysics*, *30*(1), 575–611.

Condon, J., Cotton, W., Greisen, E., Yin, Q., Perley, R., Taylor, G., & Broderick, J. (1998). The nrao vla sky survey. *The Astronomical Journal*, *115*(5), 1693.

Dahle, H., Kaiser, N., Irgens, R. J., Lilje, P. B., & Maddox, S. J. (2002). Weak gravitational lensing by a sample of x-ray luminous clusters of galaxies. i. the data set. *The Astrophysical Journal Supplement Series*, *139*(2), 313.

Dressler, A. (1980). Galaxy morphology in rich clusters-implications for the formation and evolution of galaxies. *The Astrophysical Journal*, *236*, 351–365.

Dunn, R. J., Fabian, A., & Taylor, G. (2005). Radio bubbles in clusters of galaxies. *Monthly Notices of the Royal Astronomical Society*, *364*(4), 1343–1353.

Enßlin, T. A. (2001). Reviving fossil radio plasma in clusters of galaxies by adiabatic compression in environmental shock waves. *Astronomy & Astrophysics*, *366*(1), 26–34.

Enßlin, T. A., Biermann, P. L., Klein, U., & Kohle, S. (1997). Cluster radio relics as a tracer of shock waves of the large-scale structure formation. *arXiv preprint astro-ph/9712293*.

Fanaroff, B., & Riley, J. (1974). The morphology of extragalactic radio sources of high and low luminosity. *Monthly Notices of the Royal Astronomical Society*, *167*(1), 31P–36P.

Feretti, L. (2005). Non-thermal emission from the intracluster medium. *Advances in Space Research*, *36*(4), 729–737.

Feretti, L., Dallacasa, D., Govoni, F., Giovannini, G., Taylor, G., & Klein, U. (1999). The radio galaxies and the magnetic field in abell 119. *arXiv preprint astro-ph/9902019*.

Feretti, L., Giovannini, G., Govoni, F., & Murgia, M. (2012). Clusters of galaxies: observational properties of the diffuse radio emission. *The Astronomy and Astrophysics Review*, *20*(1), 54.

Flesch, E., & Hardcastle, M. J. (2004). An all-sky optical catalogue of radio/x-ray sources. *Astronomy & Astrophysics*, *427*(1), 387–392.

Geringer-Sameth, A., & Koushiappas, S. M. (2011). Exclusion of canonical weakly interacting massive particles by joint analysis of milky way dwarf galaxies with data from the fermi gamma-ray space telescope. *Physical Review Letters*, *107*(24), 241303.

Giacintucci, S., & Venturi, T. (2009). Tailed radio galaxies as tracers of galaxy clusters. serendipitous discoveries with the gmrt. *Astronomy & Astrophysics*, *505*(1), 55–61.

Giovannini, G., Bonafede, A., Feretti, L., Govoni, F., Murgia, M., Ferrari, F., & Monti, G. (2009). Radio halos in nearby (z <0.4) clusters of galaxies. *Astronomy & Astrophysics*, *507*(3), 1257–1270.

Giovannini, G., Feretti, L., Bacchi, M., & Govoni, F. (2003). Spectral properties of radio halos. In *Matter and energy in clusters of galaxies* (Vol. 301, p. 483).

Giovannini, G., Feretti, L., Venturi, T., Kim, K.-T., & Kronberg, P. (1993). The halo radio source coma c and the origin of halo sources. *The Astrophysical Journal*, *406*, 399–406.

Giovannini, G., Tordi, M., & Feretti, L. (1999). Radio halo and relic candidates from the nrao vla sky survey. *New Astronomy*, *4*(2), 141–155.

Gitti, M., Ferrari, C., Domainko, W., Feretti, L., & Schindler, S. (2007). Discovery of diffuse radio emission at the center of the most x-ray-luminous cluster rx j1347. 5-1145. *Astronomy & Astrophysics*, *470*(3), L25–L28.

Gondolo, P., Edsjö, J., Ullio, P., Bergström, L., Schelke, M., & Baltz, E. A. (2004). Darksusy: Computing supersymmetric dark matter properties numerically. *Journal of Cosmology and Astroparticle Physics*, *2004*(07), 008.

Govoni, F., & Feretti, L. (2004). Magnetic fields in clusters of galaxies. *International Journal of Modern Physics D*, *13*(08), 1549–1594.

Govoni, F., Feretti, L., Giovannini, G., Böhringer, H., Reiprich, T., & Murgia, M. (2001). Radio and x-ray diffuse emission in six clusters of galaxies. *Astronomy & Astrophysics*, *376*(3), 803–819.

Govoni, F., Murgia, M., Feretti, L., Giovannini, G., Dallacasa, D., & Taylor, G. (2005). A2255: The first detection of filamentary polarized emission in a radio halo. *Astronomy & Astrophysics*, *430*(1), L5–L8.

Govoni, F., Murgia, M., Markevitch, M., Feretti, L., Giovannini, G., Taylor, G., & Carretti, E. (2009). A search for diffuse radio emission in the relaxed, cool-core galaxy clusters a1068, a1413, a1650, a1835, a2029, and ophiuchus. *Astronomy & Astrophysics*, *499*(2), 371–383.

Haehnelt, M. G., & Tegmark, M. (1996). Using the kinematic sunyaev-zeldovich effect to determine the peculiar velocities of clusters of galaxies. *Monthly Notices of the Royal Astronomical Society*, *279*(2), 545–556.

Harvey, D., Massey, R., Kitching, T., Taylor, A., & Tittley, E. (2015). The nongravitational interactions of dark matter in colliding galaxy clusters. *Science*, *347*(6229), 1462–1465.

Hoekstra, H., Yee, H. K. C., & Gladders, M. D. (2004). Properties of galaxy dark matter halos from weak lensing. *The Astrophysical Journal*, *606*(1), 67.

Hogg, D. W., Baldry, I. K., Blanton, M. R., & Eisenstein, D. J. (2002). The k correction. *arXiv preprint astro-ph/0210394*.

Hooper, D., & Linden, T. (2011). Origin of the gamma rays from the galactic center. *Physical Review D*, *84*(12), 123005.

Hooper, D., & Profumo, S. (2007). Dark matter and collider phenomenology of universal extra dimensions. *Physics Reports*, *453*(2), 29–115.

Huang, X., Vertongen, G., & Weniger, C. (2012). Probing dark matter decay and annihilation with fermi lat observations of nearby galaxy clusters. *Journal of Cosmology and Astroparticle Physics*, *2012*(01), 042.

Hudson, D. S., Mittal, R., Reiprich, T. H., Nulsen, P. E., Andernach, H., & Sarazin, C. L. (2010). What is a cool-core cluster? a detailed analysis of the cores of the x-ray flux-limited hiflugcs cluster sample. *Astronomy & Astrophysics*, *513*, A37.

Intema, H., Jagannathan, P., Mooley, K., & Frail, D. (2017). The gmrt 150 mhz all-sky radio survey-first alternative data release tgss adr1. *Astronomy & Astrophysics*, *598*, A78.

Jaffe, W. (1977). Origin and transport of electrons in the halo radio source in the coma cluster. *The Astrophysical Journal*, *212*, 1–7.

Jungman, G., Kamionkowski, M., & Griest, K. (1996). Supersymmetric dark matter. *Physics Reports*, *267*(5-6), 195–373.

Kellermann, K. I., & Owen, F. N. (n.d.). 13. radio galaxies and quasars.

Klamer, I., Subrahmanyan, R., & Hunstead, R. (2004). A binary system of tailed radio galaxies. *Monthly Notices of the Royal Astronomical Society*, *351*(1), 101–109.

Krawczynski, H., & Treister, E. (2013). Active galactic nuclei—the physics of individual sources and the cosmic history of formation and evolution. *Frontiers of Physics*, *8*(6), 609–629.

Lane, W., Cotton, W., van Velzen, S., Clarke, T., Kassim, N., Helmboldt, J., ... Cohen, A. (2014). The very large array low-frequency sky survey redux (vlssr). *Monthly Notices of the Royal Astronomical Society*, *440*(1), 327–338.

Large, M., Mathewson, D., & Haslam, C. (1959). A high-resolution survey of the coma cluster of galaxies at 408 mc./s. *Nature*, *183*(4676), 1663–1664.

Linden, T., Hooper, D., & Yusef-Zadeh, F. (2011). Dark matter and synchrotron emission from galactic center radio filaments. *The Astrophysical Journal*, *741*(2), 95.

Macario, G., Venturi, T., Intema, H., Dallacasa, D., Brunetti, G., Cassano, R., ... Athreya, R. (2013). 153 mhz gmrt follow-up of steep-spectrum diffuse emission in galaxy clusters. *Astronomy & Astrophysics*, *551*, A141.

Mainzer, A. K., Eisenhardt, P., Wright, E. L., Liu, F.-C., Irace, W., Heinrichsen, I., ... Duval, V. (2005). Preliminary design of the wide-field infrared survey explorer (wise). *arXiv preprint astro-ph/0508246*.

Marchegiani, P., & Colafrancesco, S. (2016). The role of dark matter sub-halos in the non-thermal emission of galaxy clusters. *Journal of Cosmology and Astroparticle Physics*, *2016*(11), 033.

Markevitch, M., Ponman, T., Nulsen, P., Bautz, M., Burke, D., David, L., ... others (2000). Chandra observation of abell 2142: Survival of dense subcluster cores in a merger. *The Astrophysical Journal*, *541*(2), 542.

Markevitch, M., & Vikhlinin, A. (2001). Merger shocks in galaxy clusters a665 and a2163 and their relation to radio halos. *The Astrophysical Journal*, *563*(1), 95.

Markevitch, M., & Vikhlinin, A. (2007). Shocks and cold fronts in galaxy clusters. *Physics Reports*, *443*(1), 1–53.

Miley, G. (1980). The structure of extended extragalactic radio sources. *Annual review of astronomy and astrophysics*, *18*(1), 165–218.

Mitchell, R., Culhane, J., Davison, P., & Ives, J. (1976). Ariel 5 observations of the x-ray spectrum of the perseus cluster. *Monthly Notices of the Royal Astronomical Society*,

175(1), 29P–34P.

Owen, F. N., & Rudnick, L. (1976). Radio sources with wide-angle tails in abell clusters of galaxies. *The Astrophysical Journal*, *205*, L1–L4.

O'Dell, S. L., Bautz, M. W., Blackwell, W. C., Butt, Y. M., Cameron, R. A., Elsner, R. F., ... others (2000). Radiation environment of the chandra x-ray observatory. In *Proc. spie* (Vol. 4140, pp. 99–110).

Pacholczyk, A. G. (1970). *Radio astrophysics*.

Peterson, J., Kahn, S., Paerels, F., Kaastra, J., Tamura, T., Bleeker, J., ... Jernigan, J. (2003). High-resolution x-ray spectroscopic constraints on cooling-flow models for clusters of galaxies. *The Astrophysical Journal*, *590*(1), 207.

Pieri, L., Lavalle, J., Bertone, G., & Branchini, E. (2011). Implications of high-resolution simulations on indirect dark matter searches. *Physical Review D*, *83*(2), 023518.

Pinkney, J., Burns, J. O., Ledlow, M. J., Gómez, P. L., & Hill, J. M. (2000). Substructure in clusters containing wide-angle-tailed radio galaxies. i. new redshifts. *The Astronomical Journal*, *120*(5), 2269.

Rees, M., & Setti, G. (1968). Model for the evolution of extended radio sources. *Nature*, *219*(5150), 127–131.

Rosswog, S., & Brüggen, M. (2007). *Introduction to high-energy astrophysics* (Vol. 37). Cambridge university press Cambridge.

Rothenflug, R., & Arnaud, M. (1985). Iron abundance in galaxy clusters. *Astronomy and Astrophysics*, *144*, 431–442.

Rubin, V. C., & Ford Jr, W. K. (1970). Rotation of the andromeda nebula from a spectroscopic survey of emission regions. *The Astrophysical Journal*, *159*, 379.

Rubin, V. C., Ford Jr, W. K., & D'Odorico, S. (1970). Emission-line intensities and radial velocities in the interacting galaxies ngc 4038-4039. *The Astrophysical Journal*, *160*, 801.

Rudaz, S., & Stecker, F. (1991). On the observability of the gamma-ray line flux from dark matter annihilation. *The Astrophysical Journal*, *368*, 406–410.

Sand, D. J., Treu, T., Ellis, R. S., & Smith, G. P. (2005). A systematic search for gravitationally lensed arcs in the hubble space telescope wfpc2 archive. *The Astrophysical Journal*, *627*(1), 32.

Sarazin, C., & Bahcall, J. (1977). X-ray line emission for clusters of galaxies. ii-numerical models. *The Astrophysical Journal Supplement Series*, *34*, 451–467.

Sasao, T., & Fletcher, A. B. (2005). Basic knowledge of radio astronomy. *Suwon: Ajou University*.

Sault, R. J., Teuben, P. J., & Wright, M. (2006). A retrospective view of miriad. *arXiv preprint astro-ph/0612759*.

Scheuer, P. (1974). Models of extragalactic radio sources with a continuous energy supply from a central object. *Monthly Notices of the Royal Astronomical Society*, *166*(3), 513–528.

Shimwell, T., Röttgering, H., Best, P. N., Williams, W., Dijkema, T., De Gasperin, F., ... others (2017). The lofar two-metre sky survey-i. survey description and preliminary data release. *Astronomy & Astrophysics*, *598*, A104.

Sunyaev, R., & Zel'dovich, Y. B. (1972). The observations of relic radiation as a test of the nature of x-ray radiation from the clusters of galaxies. *Comments on Astrophysics and Space Physics*, *4*, 173.

Sunyaev, R., & Zel'dovich, Y. B. (1970). R. sunyaev ya.-b. zel'dovichand, astrophys. j. suppl. ser. 7, 3 (1970). *Astrophys. J. Suppl. Ser.*, *7*, 3.

Thierbach, M., Klein, U., & Wielebinski, R. (2003). The diffuse radio emission from the coma cluster at 2.675 ghz and 4.85 ghz. *Astronomy & Astrophysics*, *397*(1), 53–61.

Tozzi, P., & Norman, C. (2001). The evolution of x-ray clusters and the entropy of the intracluster medium. *The Astrophysical Journal*, *546*(1), 63.

Tribble, P. C. (1993). Radio haloes, cluster mergers, and cooling flows. *Monthly Notices of the Royal Astronomical Society*, *263*(1), 31–36.

Trippe, S. (2014). Polarization and polarimetry: A review. *arXiv preprint arXiv:1401.1911*.

Urry, C. M., & Padovani, P. (1995). Unified schemes for radio-loud active galactic nuclei. *Publications of the Astronomical Society of the Pacific*, *107*(715), 803.

Vazza, F., Brüggen, M., Gheller, C., & Wang, P. (2014). On the amplification of magnetic fields in cosmic filaments and galaxy clusters. *Monthly Notices of the Royal Astronomical Society*, *445*(4), 3706–3722.

Vazza, F., Brüggen, M., Wittor, D., Gheller, C., Eckert, D., & Stubbe, M. (2016). Constraining the efficiency of cosmic ray acceleration by cluster shocks. *Monthly Notices of the Royal Astronomical Society*, *459*(1), 70–83.

Velander, M., van Uitert, E., Hoekstra, H., Coupon, J., Erben, T., Heymans, C., ... others (2013). Cfhtlens: the relation between galaxy dark matter haloes and baryons from weak gravitational lensing. *Monthly Notices of the Royal Astronomical Society*, *437*(3), 2111–2136.

Venturi, T., Giacintucci, S., Cassano, R., Brunetti, G., Dallacasa, D., Macario, G., ... Athreya, R. (2009). The gmrt radio halo survey and low frequency follow-up. *arXiv preprint arXiv:0903.2934*.

Venturi, T., Giacintucci, S., Dallacasa, D., Cassano, R., Brunetti, G., Bardelli, S., & Setti, G. (2008). Gmrt radio halo survey in galaxy clusters at z= 0.2–0.4-ii. the ebcs clusters and analysis of the complete sample. *Astronomy & Astrophysics*, *484*(2), 327–340.

Venturi, T., Giacintucci, S., Dallacasa, D., Cassano, R., Brunetti, G., Macario, G., & Athreya, R. (2013). Low frequency follow up of radio haloes and relics in the gmrt radio halo cluster survey. *Astronomy & Astrophysics*, *551*, A24.

Vikhlinin, A., Markevitch, M., & Murray, S. (2001). Chandra estimate of the magnetic field strength near the cold front in a3667. *The Astrophysical Journal Letters*, *549*(1), L47.

Weisskopf, M., Brinkman, B., Canizares, C., Garmire, G., Murray, S., & Van Speybroeck, L. (2002). An overview of the performance and scientific results from the chandra x-ray observatory. *Publications of the Astronomical Society of the Pacific*, *114*(791), 1.

Widrow, L. M. (2002). Origin of galactic and extragalactic magnetic fields. *Reviews of Modern Physics*, *74*(3), 775.

Willson, M. (1970). Radio observations of the cluster of galaxies in coma berenices—the 5c4 survey. *Monthly Notices of the Royal Astronomical Society*, *151*(1), 1–44.

Wright, E. L., Eisenhardt, P. R., Mainzer, A. K., Ressler, M. E., Cutri, R. M., Jarrett, T., ... others (2010). The wide-field infrared survey explorer (wise): mission description and initial on-orbit performance. *The Astronomical Journal*, *140*(6), 1868.

Zhang, Y.-Y., Andernach, H., Caretta, C. A., Reiprich, T. H., Böhringer, H., Puchwein, E., ... Girardi, M. (2011). Hiflugcs: Galaxy cluster scaling relations between x-ray luminosity, gas mass, cluster radius, and velocity dispersion. *Astronomy & Astrophysics*, *526*, A105.

Zwicky, F. (1933). Helvetic physica acta 6, p. 110.

Zwicky, F., & Herzog, E. (1968). *Catalogue of galaxies and of clusters of galaxies* (Vol. 4). Caltech.